### Title

Effect of point bar development on the local force balance governing flow in a simple, meandering gravel bed river




### Journal

Journal of Geophysical Research, 116(F1)

### ISSN

0148-0227



### Authors

Legleiter, CJ
Harrison, LR
Dunne, T



### Publication Date

2011-03-01

### DOI

10.1029/2010jf001838

# Effect of point bar development on the local force balance governing flow in a simple, meandering gravel bed river

C. J. Legleiter,[1] L. R. Harrison,[2] and T. Dunne[3]

Received 30 July 2010; revised 7 November 2010; accepted 19 November 2010; published 5 February 2011.

[1] The patterns of depth, velocity, and shear stress that direct a river's morphologic evolution are governed by a balance of forces. Analyzing these forces, associated with pressure gradients, boundary friction, channel curvature, and along- and across-stream changes in fluid momentum driven by bed topography, can yield insight regarding the establishment and maintenance of stable channel forms. This study examined how components of the local force balance changed as a meandering channel evolved from a simple, flat-bedded initial condition to a more complex bar-pool morphology. A numerical flow model, constrained by measurements of velocity and water surface elevation, characterized the flow field for four time periods bracketing two floods. For each time increment, runs were performed for discharges up to bankfull, and individual force balance components were computed from model output. Formation and growth of point bars enhanced topographic steering effects, which were of similar magnitude to the pressure gradient and centrifugal forces. Convective accelerations induced by the bar reduced the cross-stream pressure gradient, intensified flow toward the outer bank, and routed sediment around the upstream end of the bar. Adjustments in the flow field thus served to balance streamwise transport along the inner bank onto the bar and cross-stream transport into the pool. Even in the early stages of bar development, topographically driven spatial gradients in velocity played a significant role in the force balance at flows up to bankfull, altering the orientation of the shear stress and sediment transport to drive bar growth.

**Citation:** Legleiter, C. J., L. R. Harrison, and T. Dunne (2011), Effect of point bar development on the local force balance governing flow in a simple, meandering gravel bed river, *J. Geophys. Res.*, *116*, F01005, doi:10.1029/2010JF001838.

## 1. Introduction

[2] To model bed material transport and channel change, spatial patterns of depth, velocity, and boundary shear stress must be predicted accurately as they evolve in concert with the morphology. An effective means of achieving this objective is to consider the balance of forces that governs the flow field. In meander bends, the relevant forces arise from gradients in pressure, frictional shear along the channel boundary, centrifugal acceleration due to curvature, and along- and across-stream changes in fluid momentum driven by the bed topography. An important component of the local force balance, the one ultimately responsible for sediment movement, is the boundary shear stress. Because the magnitude and orientation of shear stress vectors are influenced by the other forces comprising this balance, understanding individual force balance components and their interactions can help to explain stress fields, associated patterns of erosion and deposition, and the resulting topographic adjustments. A systematic examination of the local force balance can thus yield insight regarding the feedbacks between hydraulics and morphology that occur during the initial development and subsequent maintenance of stable channel forms.

[3] In this study, we describe the evolution of point bars along a simple, meandering gravel bed river, document their influence on patterns of bend flow, and quantify the resulting adjustments in individual components of the local force balance. This detailed characterization of the flow field is then used to guide interpretation of the observed changes in channel morphology. Although this investigation makes use of a numerical flow model, our focus is not on the modeling per se, but rather on examining more closely some of the key form-process interactions that must be represented accurately by any such model. In essence, we seek insight regarding channel morphodynamics in an indirect manner by mapping force balance components at different stages in

[1]Department of Geography, University of Wyoming, Laramie, Wyoming, USA.
[2]Institute for Computational Earth System Science, University of California, Santa Barbara, California, USA.
[3]Bren School of Environmental Science and Management and Department of Earth Science, University of California, Santa Barbara, California, USA.


0148-0227/11/2010JF001838

the evolution of the reach and using that information to explain the measured channel changes in terms of the mechanics governing the flow during each stage of bar development.

[4] Efforts to understand the dynamics of meandering streams have produced a vast body of literature, summarized in recent reviews by *Seminara* [2006], *Camporeale et al.* [2007], and *Seminara* [2010]. Early work described how the cross-stream pressure gradient and centrifugal acceleration give rise to secondary circulation patterns that play a key role in establishing the flow field and bed topography characteristic of sinuous channels [e.g., *Engelund*, 1974]. These processes act to transfer momentum across the channel toward the outer bank, and *Ikeda et al.* [1981] linked the near-bank flow velocity to the rate of bank erosion and lateral channel migration. Building upon this seminal paper, many workers have examined the relationship between bend flow and planform evolution [*Camporeale et al.*, 2007, and references therein]. For example, *Blondeaux and Seminara* [1985] performed a linear stability analysis that revealed a resonance between migrating "free" bars typical of alternate bar channels and "forced" (point) bars associated with channel bends. Similar techniques have also been used to investigate secondary currents [*Johannesson and Parker*, 1989]. Linear models of this kind provide efficient analytical solutions that have been widely used to support numerical [e.g., *Howard and Knutson*, 1984; *Crosato*, 2009], theoretical [e.g., *Struiksma et al.*, 1985; *Lanzoni and Seminara*, 2006], and empirical [e.g., *Constantine et al.*, 2009] investigations of meander dynamics.

[5] These linear models are subject to an important limitation, however. They are strictly only valid in the case of low curvature and slowly varying bed topography [*Camporeale et al.*, 2007]. Fully nonlinear models [e.g., *Smith and McLean*, 1984; *Blanckaert and de Vriend*, 2003], in contrast, have fewer geometric restrictions and make a more explicit connection between the flow field and the morphology at the scale of an individual channel bend, but at a much greater computational cost [*Camporeale et al.*, 2007]. Another, more recent modeling strategy involves two- and three-dimensional computational fluid dynamics [e.g., *Shimizu et al.*, 1990; *Ferguson et al.*, 2003; *Duan and Julien*, 2005; *Ruther and Olsen*, 2007]. These numerical flow simulations have been coupled with models of bed material transport [e.g., *Li et al.*, 2008; *Vasquez et al.*, 2008] and bank erosion [e.g., *Mosselman*, 1998; *Darby et al.*, 2002; *Rinaldi et al.*, 2008] as a means of predicting the evolution of channel form [e.g., *Fischer-Antze et al.*, 2008].

[6] Different types of models employ different kinds of approximations, and the significance of certain terms in the momentum equations has been the subject of long-standing debate [e.g., *Dietrich and Whiting*, 1989]. For several decades this issue has been examined via flume experiments [*Yen and Yen*, 1971; *Blanckaert*, 2010], theoretical derivations [*Smith and McLean*, 1984], numerical modeling [*Nelson and Smith*, 1989a], and field studies [*Dietrich and Smith*, 1983; *Whiting and Dietrich*, 1991], and yet a number of controversies persist. For example, the work of *Smith and McLean* [1984] and *Nelson and Smith* [1989a] indicated that earlier models [e.g., *Engelund*, 1974] tended to underestimate the influence of downstream varying bed topography on spatial gradients in flow velocity. *Ikeda et al.* [1981] and *Johannesson and Parker* [1989] also downplayed the role of bar-pool channel morphology as a control on flow patterns by treating convective accelerations as second-order effects (i.e., as perturbations of the mean behavior). Instead, the influence of point bar geometry was accounted for by means of a calibration parameter (i.e., bank erodibility coefficient), raising the question as to whether these widely used models of planform evolution accurately portray the advection of the high-velocity core toward the outside of the bend and its effect on bank erosion and channel migration.

[7] In contrast, explicitly considering the effects of the point bar on the flow field can highlight the effects of bar development on shear stress in the adjacent pool, erosion of the outer bank, and hence the dynamics of curved channels. For example, *Lancaster and Bras* [2002] produced reasonable simulations of meander evolution using a model based on transverse flow acceleration due to bed topography and hypothesized that this type of cross-stream momentum transfer exerts a primary control on bank erosion. Applying this topographic steering model to a Dutch river, *de Moor et al.* [2007] found close agreement between predicted patterns of lateral channel migration and the observed spatial distribution of erosive banks and measured migration rates.

[8] Although this issue of topographically driven convective accelerations of the flow might seem quite narrow, the topic is pertinent to sediment transfer and storage, bank erosion, and lateral channel migration and thus has significant implications for the form and behavior of meandering rivers. In this study, we focus on a systematic consideration of the force balance governing the flow field at the scale of an individual bar-pool unit. This analysis is performed within the theoretical framework proposed by *Smith and McLean* [1984], a model that has only been evaluated in a few natural rivers spanning a fairly limited range of conditions [*Dietrich et al.*, 1979; *Dietrich and Smith*, 1983; *Dietrich and Whiting*, 1989; *Whiting and Dietrich*, 1991; *Whiting*, 1997]. Here, we build upon these efforts by examining a larger, gravel bed river along which we have observed the formation and growth of point bars. Although previous investigations have documented the development of alternate bar sequences in straight channels [e.g., *Lewin*, 1976; *Lisle et al.*, 1991], our unique field site, a recently reconstructed river that featured an engineered meandering planform but initially lacked bars, allowed the effect of bar growth to be decoupled from that of meander initiation. Similarly, whereas earlier work by Dietrich and Whiting considered a single, static morphology, a time series of survey data enabled us to examine the effects of bar development on the local force balance and assess the extent to which the relative magnitude of topographic steering effects changed as the bar-pool morphology evolved. Moreover, unlike prior studies that considered only one or two discharges well below bankfull, we used a calibrated numerical flow model to quantify the stage dependence of the force balance for flows up to bankfull.

[9] By documenting point bar development, quantifying the corresponding changes in the flow field, and interpreting the measured morphologic and modeled hydraulic adjustments in terms of the local force balance, we seek to understand how the flow field and morphology interact as a

simple, flat-bedded meandering channel evolves toward a more complex bar-pool topography. Such a scenario might arise in rivers that have experienced large floods and/or massive, episodic sediment inputs [e.g., *Pitlick*, 1993; *Madej*, 1999]. The widening and sedimentation associated with these events often result in channel expansion and simplification [e.g., *Meyer*, 2001]. The transport capacity of the enlarged channel would thus be reduced under more typical flow conditions, and a series of hydraulic and morphologic adjustments would ensue so as to achieve a new balance between sediment supply and transport capacity [e.g., *Madej*, 2001; *Madej et al.*, 2009]. An analogous sequence of changes might be expected to occur as a river that has been simplified during restoration gradually develops more complex, natural topography featuring bar forms of higher amplitude. Storage of bed material in bars is often a salient feature of a channel's response to changes in the controlling factors of discharge and sediment supply. The goal of this study was to examine the nature of this response within a force balance framework, focusing on the role of topographic steering effects associated with the formation and growth of point bars. More specifically, we address the following research questions:

[10] 1. Are topographically induced convective accelerations important only in relatively shallow flows, or does this component of the local force balance take on a similar magnitude as the pressure gradient, boundary shear stress, and curvature-driven centrifugal acceleration in large gravel bed rivers at bankfull flow?

[11] 2. How does the relative importance of individual force balance components, including topographic steering effects, change over time as point bars develop?

[12] 3. How and to what extent does the significance of these forces vary as a function of flow stage?

## 2. Methods

[13] To examine these issues, we combined field- and modeling-based approaches, using measurements of topography, water surface elevation, and bed material grain size to parameterize a quasi-three-dimensional numerical flow model. The difficulty of obtaining measurements of sufficient accuracy, resolution, and spatial density to evaluate individual force balance terms is well documented and has restricted prior field studies to short reaches of small streams [e.g., *Dietrich and Smith*, 1983; *Whiting and Dietrich*, 1991]. A modeling approach, well-constrained by field data, is more readily applicable to a broader range of channels and flows and enables continuous characterization of the flow field. The latter point is a distinct advantage: the spatial derivatives of depth, velocity, and water surface elevation that appear in the momentum equations can be calculated directly from spatially distributed model output, whereas these quantities would be difficult to evaluate precisely from field measurements, especially for morphogenetically significant flows in gravel bed rivers.

[14] That our results were derived from model predictions rather than measurements might be viewed as a shortcoming, however. Although we have not directly measured the quantities involved in the local force balance, as some earlier workers painstakingly have done [*Dietrich and Smith*, 1983; *Whiting and Dietrich*, 1991], field data were collected to calibrate and, to an extent, verify the model used to predict these quantities. Under the incremental approach adopted herein, model output was used only to reconstruct the individual forces governing the modeled flow field. For each step in a topographic time series that documented significant changes in channel morphology, we (1) used the model to characterize the flow field; (2) computed individual terms in the momentum equations from the model output; (3) examined components of the local force balance and associated patterns of boundary shear stress; and (4) inferred a process-based explanation for the morphologic adjustments that might be expected to occur under these topographic and hydraulic conditions.

[15] By considering topographic data from successive time periods, we were able to use the flow model, and its decomposition into specific forces, to interpret how the hydraulic patterns observed during one time period produced the morphology observed at a later date. Although more complex 2-D and 3-D computational fluid dynamics models have been developed and used to simulate sediment transport and morphologic evolution in rivers [e.g., *Li et al.*, 2008; *Fischer-Antze et al.*, 2008], a relatively simple, quasi-3-D model in which the bed and banks were fixed was sufficient for our purposes here. The objective of this study was not to evaluate a particular numerical model or to use such a model to predict channel change. Instead, we focused on using model output to gain insight regarding the forces governing the flow field at different stages of bar development and hence improve our understanding of the basic processes by which these changes occur.

### 2.1. Study Area and Field Data

[16] This study took place along the recently reconstructed Robinson Reach of the lower Merced River in California's Central Valley (Figure 1). Beginning in 2001, the channel was engineered to improve salmon spawning habitat conditions, with gross dimensions, grain size, and single-thread, meandering planform designed to ensure mobility of spawning gravels under the regulated, postdam hydrologic regime while maintaining a stable morphology [*California Department of Water Resources* (*CDWR*), 2001]; attributes of the reconstructed channel are summarized in Table 1. Table 2 lists values of a topographic relief ratio that provided not only a consistent measure of the potential influence of channel morphology on the flow field for the various time periods and discharges we considered but also a means of comparing our work to previous studies. Following *Whiting* [1997], we computed this ratio by dividing the local maximum depth within each meander bend by the mean depth for the cross section along which this maximum occurred. Topographic relief on the Merced ranged from 1.71 to 2.03 over time as point bars developed, lower than the 2.25 and 2.10 reported by *Whiting* [1997] for a midchannel bar at low and intermediate flow stages, respectively, but similar to the value of 1.8 for the point bar examined by *Dietrich and Smith* [1983]. The reengineered Robinson Reach provided an opportunity to observe the development of more complex morphology from a simple, known initial condition. Similar studies have been performed in artificially straightened channels [e.g., *Lewin*, 1976], but the sinuous planform of our field site allowed

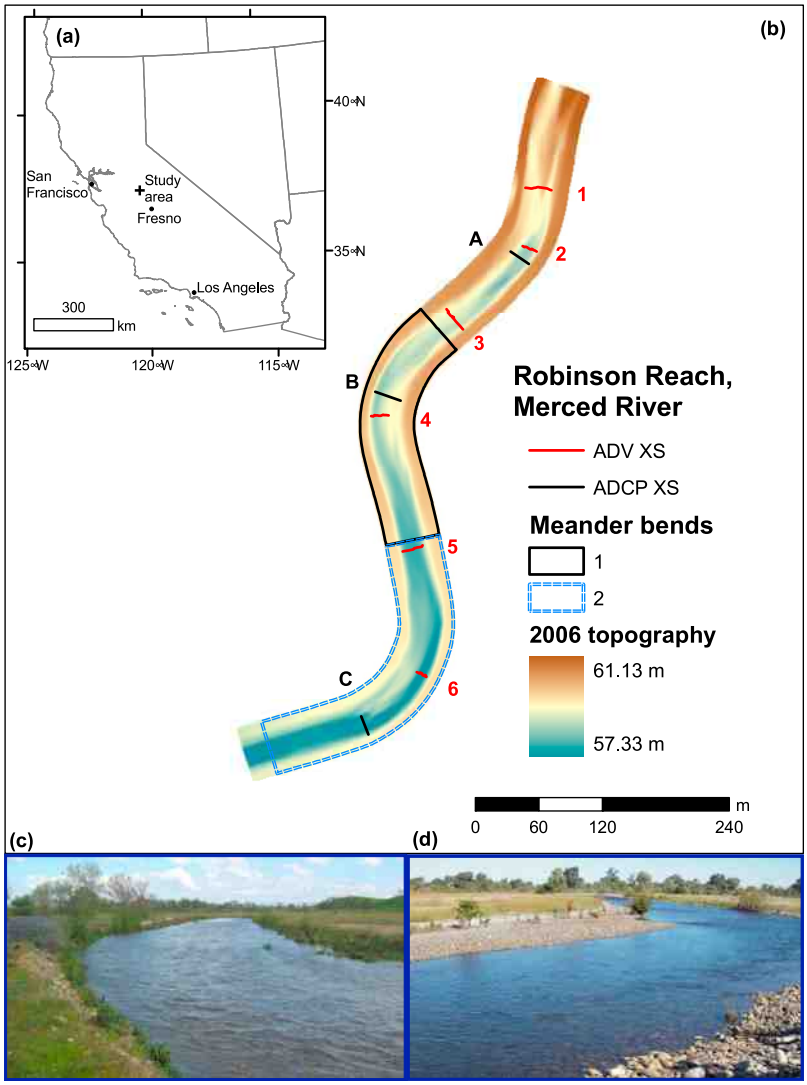


**Figure 1.** (a) Location of the study area on the Robinson Reach of the Merced River. (b) Bed topography of the reach. Also indicated are the cross sections (numbers) at which point measurements of velocity were made at a low flow of 6.4 $m^3/s$ (Figure 7), the transects (letters) where an ADP was used to record velocity profiles at a nearly bankfull discharge of 42.5 $m^3/s$ (Figure 8), and the two meander bends upon which this study focused. The photos illustrate (c) the initial configuration of the meander bends, with wide, flat-bottomed pools lacking bars, and (d) point bars deposited during a sustained overbank flood event that occurred in 2005.

us to examine the effects of point bar development in a channel in which appreciable curvature had already been established (via restoration). In previous investigations of initially straight channels, these effects were confounded with those of alternate bar formation and meander initiation. Another advantage of the Robinson Reach was that many of the effects of particle arrangement and microtopography that complicate roughness characterization and shear stress estimation in more natural streams [e.g., *Ergenzinger*, 1992] were absent, which allowed us to concentrate on larger-scale effects during the gradual evolution of this relatively smooth, simple channel. The Merced thus represented a true-scale river, with some of the convenient features of a flume, in which we could examine the effects of point bar development on the local force balance.

**Table 1.** Channel Characteristics for the Robinson Reach of the Merced River[a]

| Characteristic | Value |
|---|---|
| Mean bankfull width | 29.2 m |
| Mean bankfull depth | 1.01 m |
| Channel bed slope | 0.0025 |
| $D_{16}$ | 32 mm |
| $D_{50}$ | 57 mm |
| $D_{84}$ | 95 mm |
| Sinuosity | 1.16 |
| Meander wavelength | 2010 m |
| Bend apex radius of curvature | 71.4 m |

[a] $D_x$ denotes the percentile of the bed material grain size distribution for which $x$ percent are finer.

**Table 2.** Values of the Topographic Relief Ratio[a]

| Time Period | Discharge ($m^3/s$) | Bend 1 | Bend 2 |
|---|---|---|---|
| Initial | 42.5 | 1.65 | 1.71 |
| Pre-flood 1 | 42.5 | 1.53 | 1.67 |
| Between floods | 42.5 | 1.79 | 1.90 |
| Post-flood 2 | 42.5 | 1.75 | 2.03 |
| Post-flood 2 | 42.5 (bankfull) | 1.75 | 2.03 |
| Post-flood 2 | 32.6 (3/4 bankfull) | 1.76 | 2.08 |
| Post-flood 2 | 6.4 (base flow) | 1.93 | 2.02 |

[a]Defined as the ratio of the local maximum depth to the section-averaged mean depth for the cross section at which the maximum depth occurs for the two bends considered in this study. Values for each of the four time periods at bankfull flow and for three different discharges for the post-flood 2 topography are reported.

[17] After construction was completed in February 2002, the Robinson Reach experienced low discharges punctuated by short, regulated pulse flows that did not exceed the design bankfull discharge. Nevertheless, tracer studies and bed load measurements conducted by the California Department of Water Resources (CDWR) indicated that the bed was partially mobile during this period [*CDWR*, 2006]. Flows capable of transporting large amounts of bed material and modifying channel form first occurred in March 2005 (Figure 2). This event inundated the broad, low-relief, largely unvegetated floodplain, had a peak discharge of 120 $m^3/s$, and remained above bankfull stage for 90 days as water was gradually released from a reservoir 28 km upstream. A similar flood occurred in 2006, with a greater peak discharge of 142 $m^3/s$ and longer duration of above bankfull flow (142 days).

[18] The initial condition of the reconstructed channel and the river's response to these two periods of sustained high flow were documented via a time series of topographic data. The CDWR provided an "as-built" survey, and we performed more detailed surveys bracketing the two events (Figure 2). We used a total station to measure cross sections spaced approximately every quarter channel width, with a typical cross-stream point spacing of 2–3 m (0.05–0.1 bankfull widths); additional points were surveyed along breaks in slope, such as the top and base of the bank, and in areas of more complex topography. The as-built survey was less detailed, with cross sections located approximately every channel width and 3–4 m between measurements along each transect. We refer to these four data sets as the initial (2002), pre-flood 1 (March 2005), between floods (October 2005), and post-flood 2 (November 2006) surveys.

[19] Additional field data were collected to support our hydraulic modeling efforts. Following the second flood event, water surface profiles were surveyed at discharges (recorded at a gage 4 km upstream of the Robinson Reach) of 42.5 $m^3/s$, a flow of sufficient magnitude to just overtop the bank in a few places; 32.5 $m^3/s$, approximately 75% of bankfull; and 6.4 $m^3/s$, representing base flow conditions. To parameterize roughness, we characterized the bed material grain size distribution using pebble counts conducted using a sampling grid and grain size template along 12 cross sections distributed throughout the 0.81 km reach depicted in Figure 1.

[20] To assess the accuracy of model predictions across a range of discharges, two sets of velocity field data were acquired during the post-flood 2 time period, after the bars had developed. The first consisted of point measurements obtained at a low flow of 6.4 $m^3/s$ along the six numbered transects in Figure 1. At each sampling location, a SonTek FlowTracker acoustic Doppler velocimeter (ADV) was oriented perpendicular to the channel cross section, positioned at a height above the bed equal to 40% of the local flow depth, and deployed for a period of 60 s at a sampling frequency of 1 Hz. The time average of these measurements

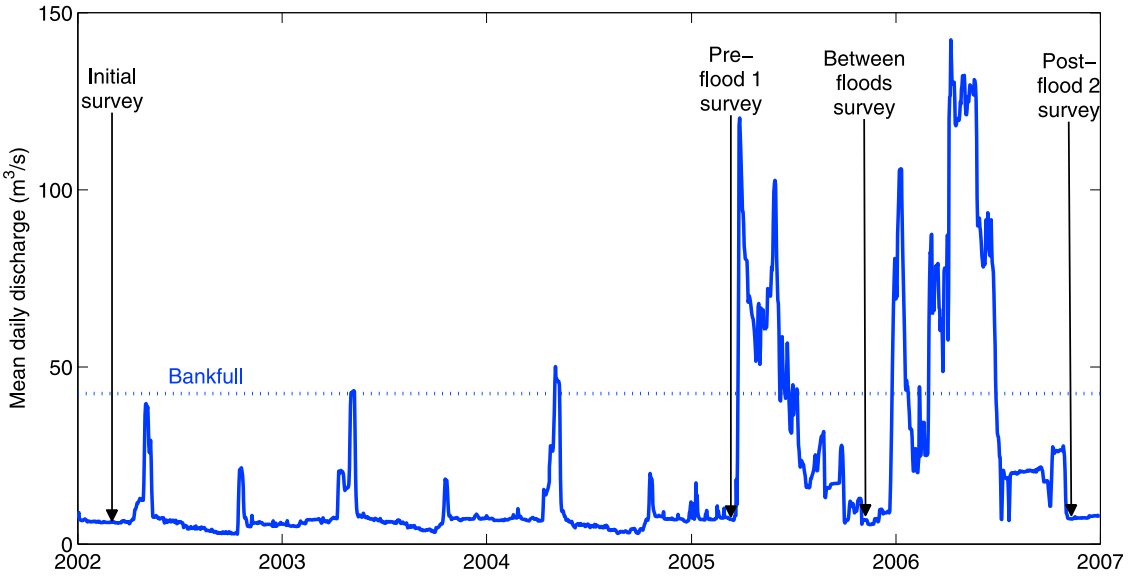


**Figure 2.** Hydrograph for the Merced River since completion of the Robinson Reach restoration project. The dates of topographic data collection are indicated.

**Table 3.** Description of Velocity Data Recorded With a SonTek ADP and Used to Assess the Accuracy of Model Predictions at a Discharge of 42.5 $m^3/s$

| Parameter | Value |
|---|---|
| Sampling duration | 120 s |
| Averaging interval | 5 s |
| Vertical cell size | 0.15 m |
| Sensor depth | 0.10 m |
| Blanking distance | 0.20 m |
| Number of cells | Depends on local depth (up to 20) |
| Number of verticals | |
| Transect A | 18 |
| Transect B | 26 |
| Transect C | 15 |

provided an estimate of the depth-averaged velocity, under an assumed logarithmic vertical profile, comparable to the output from the flow model described below. The FlowTracker recorded velocities in three dimensions, but potential misalignment between the ADV probe and the axes of the coordinate system employed by the model precluded direct comparison of observed and predicted velocity components. Instead, only velocity magnitudes (i.e., resultant of the streamwise and cross-stream components), denoted by $\langle \mathbf{u} \rangle$, were considered; a rotation of the velocity measurements, which would have required more precise information on probe orientation than was provided by the available instrumentation, was thus not necessary.

[21] Velocity data were also acquired under high-flow conditions, at a discharge of 42.5 $m^3/s$, by deploying a SonTek acoustic Doppler profiler (ADP) along the three cross sections indicated by letters in Figure 1. This instrument provided a more thorough description of the flow field by recording three-dimensional velocities for a series of vertical profiles distributed across the channel; details regarding these measurements are provided in Table 3. For each location along these transects, time-averaged velocities were computed for each cell of the vertical profile and their mean calculated to obtain a depth-averaged velocity comparable to model predictions. As with the ADV data, due to potential uncertainties related to sensor orientation relative to the model's coordinate system, we did not evaluate individual velocity components; only velocity magnitudes computed from the ADP measurements were compared to model predictions of $\langle \mathbf{u} \rangle$. Also, because of the ADP's sensor depth and blanking distance, reliable velocity data could not be obtained along the shallow margins of the channel where flow depths were less than 0.3 m.

### 2.2. Flow Modeling

[22] For each increment of our topographic time series, we used the Flow and Sediment Transport for Morphological Evolution of Channels (FaSTMECH) computational model, developed by the U.S. Geological Survey [*Nelson and Smith*, 1989b; *Nelson and McDonald*, 1996; *Lisle et al.*, 2000; *Nelson et al.*, 2003; *Barton et al.*, 2005], to obtain spatially distributed predictions of water surface elevation, flow depth and velocity, and boundary shear stress. This quasi-three-dimensional model consists of two, weakly coupled components. The first involves numerical solution of vertically and Reynolds-averaged equations representing the conservation of mass and momentum, expressed in a channel-centered orthogonal curvilinear coordinate system (section 2.3). The second component of FaSTMECH is a vertical structure submodel that accounts for secondary circulation by determining the vertical distribution of velocity both along and across the streamlines of the vertically averaged flow. The vertically averaged part of the model takes as input bed topography, discharge, and roughness (specified in terms of drag coefficients, as described below) and calculates water surface elevations and the downstream and cross-stream components of both the depth-averaged velocity and the boundary shear stress. Results from the vertically averaged model are then used as input to the vertical structure submodel, along with a function describing the vertical distribution of eddy viscosity between the bed and the water surface. FaSTMECH assumes that this distribution is parabolic for the lower 20% of the flow depth and constant for the upper portion of the water column, which results in a velocity profile that is logarithmic near the bottom and parabolic well away from the bed [*Rattray and Mitsuda*, 1974]. The vertical structure submodel calculates downstream and cross-stream components of velocity at discrete points in the vertical and thus provides information on the structure of secondary flows and the effects of secondary circulation on the boundary shear stress field.

[23] The FaSTMECH model assumes that (1) the flow is steady and hydrostatic (i.e., vertical accelerations are negligible); (2) turbulence can be represented by relating Reynolds stresses to shears via an isotropic, vertically averaged eddy viscosity; and (3) bottom stresses associated with the interaction of lateral and normal stresses with a sloping channel boundary are negligible relative to bed stresses associated with vertical shears, which are related to the vertically averaged velocities via a simple drag closure; the same type of closure is also used for lateral stresses near steep banks. Numerical solution involves a finite difference algorithm implemented on a regular, curvilinear grid created by digitizing a channel centerline and specifying the number of streamwise and cross-stream nodes. The model uses an iterative differential relaxation technique to satisfy conservation of both mass and momentum to a high degree of accuracy throughout the computational grid. For additional detail regarding the FaSTMECH model, including the underlying equations and a formal scaling analysis thereof, the interested reader is referred to *Nelson and Smith* [1989a, 1989b] and *Nelson and McDonald* [1996].

[24] In this study, all model runs were based on a common centerline and grid, illustrated in Figure 3, consisting of 779 nodes along the reach and 51 nodes across the channel, with a consistent grid node spacing of 1.02 m in each direction. For each time period, bed elevations at model grid nodes were predicted from survey data using the geostatistical techniques described by *Legleiter and Kyriakidis* [2006, 2008]. Model runs were performed for discharges of 42.5, 32.5, and 6.4 $m^3/s$, and water surface profiles surveyed at each of these flows were used to define the downstream stage boundary condition for each run. Initial conditions for the model were specified by performing one-dimensional hydraulic calculations, based on the known discharge, downstream stage, and calibrated drag coefficient (see below), to determine a water surface elevation at the upstream end of the computational domain. The two bends

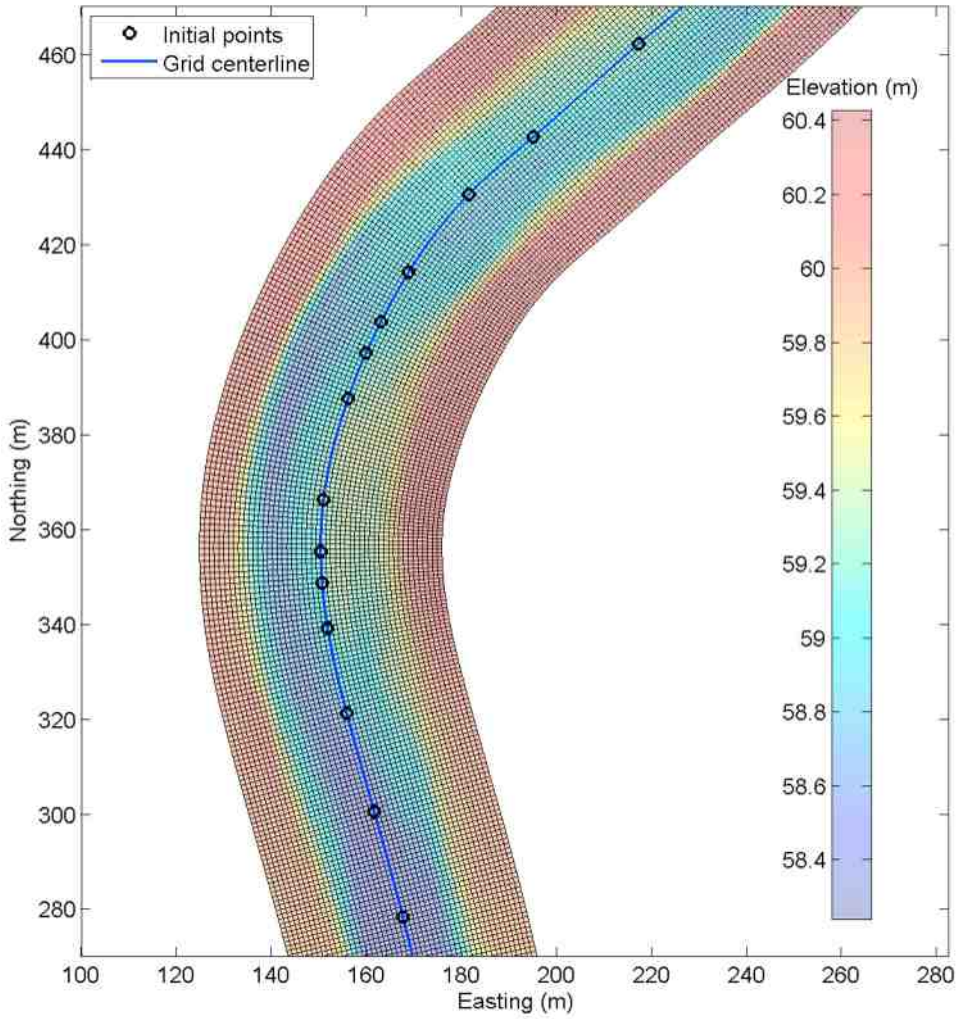


**Figure 3.** Original digitized centerline points, interpolated centerline, and computational grid employed by the FaSTMECH numerical flow model. Only a subset of the model domain, corresponding to bend 1, is shown here. Topography is from the post-flood 2 survey.

we examined in detail were located a sufficient distance downstream from the entrance to the modeled reach that the simulated flow conditions in these bends were insensitive to the initial conditions specified at the inlet.

[25] FaSTMECH parameterizes hydraulic roughness in terms of drag coefficients, denoted by $C_d$. Following *Lisle et al.* [2000] and *May et al.* [2009], we assumed that flow resistance was dominated by grain drag; given the lack of bed forms and small bed slopes along this gravel reach, form drag was considered negligible. Even if form drag were present, its effect would have been removed uniformly over the entire reach, leaving unchanged the spatial patterns of depth, velocity, and shear stress upon which our force balance analysis was based. Initially, drag coefficients were assumed to be spatially constant and flow resistance was calibrated by determining a single $C_d$ that produced close agreement between water surface elevations predicted by the model and those measured in the field. We developed a numerical optimization routine to identify a $C_d$ value that minimized the discrepancy, expressed as a root mean square error (RMSE), between predicted and observed water surface elevations. At each step in this iterative procedure, the lateral eddy viscosity (*LEV*) parameter used to represent momentum exchange due to turbulence not generated at the bed was calculated as [*Barton et al.*, 2005]

$$LEV = 0.01 \times \mathbf{u}_{avg} \times h_{avg} \quad (1)$$

where $\mathbf{u}_{avg}$ and $h_{avg}$ denote reach averages of the depth-averaged velocity and flow depth, respectively. To assess the model's sensitivity to this parameter, we used the final, optimal drag coefficient to perform runs with *LEV* values of 0.5, 0.75, 1.25, and 2 times the calculated *LEV* and found that differences in predicted velocities were negligibly small over this range.

[26] The calibrated, constant $C_d$ was then used to perform a second set of model runs for which flow resistance was dependent upon the local flow depth and thus varied spatially. For these runs, we first specified the roughness length as $z_0 = 0.1D_{84}$ [*Whiting and Dietrich*, 1990] using the reach-averaged $D_{84}$ grain size of 0.095 m and then used local flow

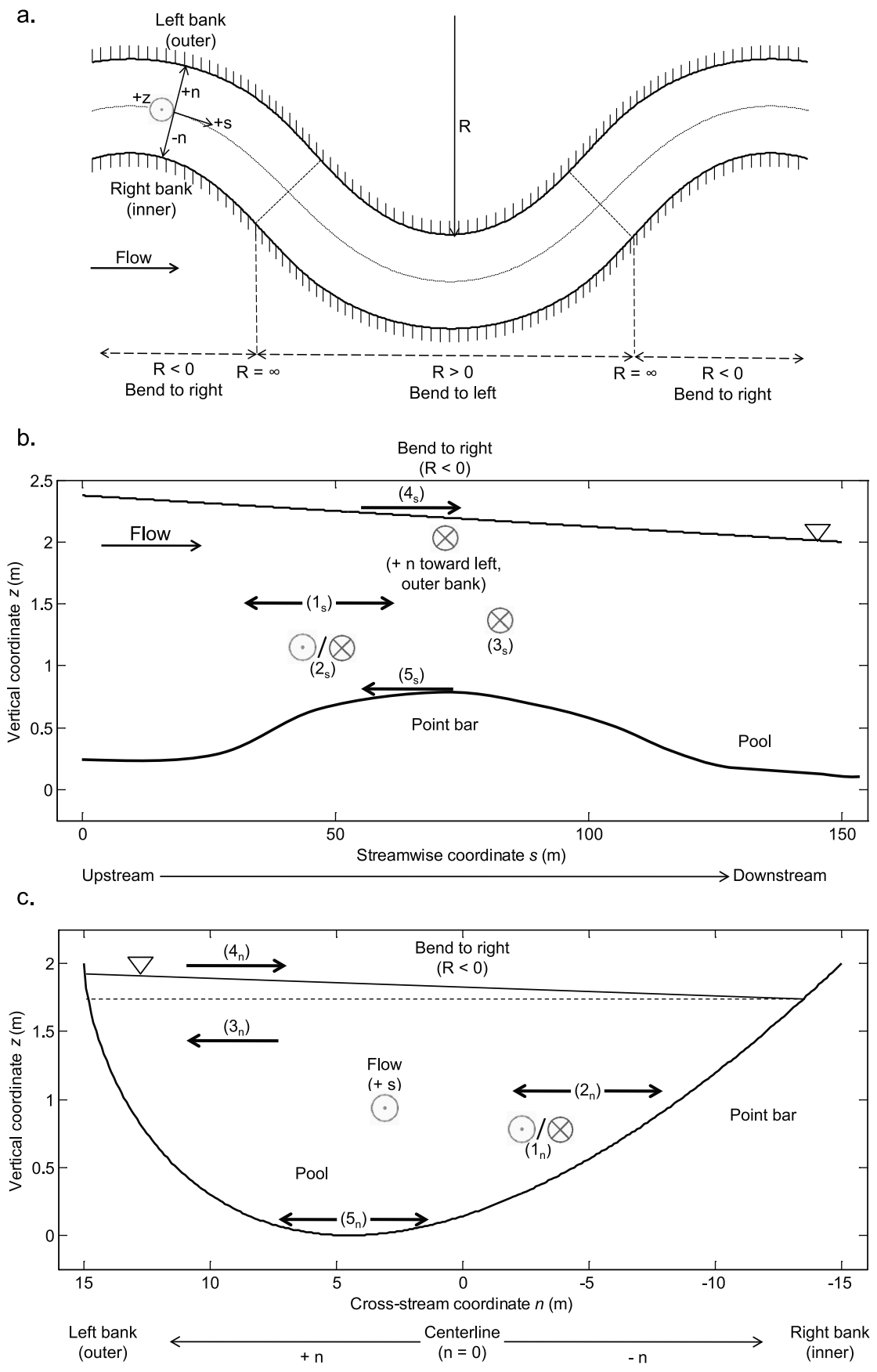
a.
Left bank
(outer)
+z
+n
+s
-n
R
Right bank
(inner)
Flow
R < 0
Bend to right
R = ∞
R > 0
Bend to left
R = ∞
R < 0
Bend to right
b.
Bend to right
(R < 0)
(4s)
Flow
(+ n toward left,
outer bank)
(1s)
(3s)
(2s)
(5s)
Point bar
Pool
Vertical coordinate z (m)
Streamwise coordinate s (m)
Upstream
Downstream
c.
(4n)
Bend to right
(R < 0)
(3n)
Flow
(+ s)
(2n)
(1n)
Point bar
Pool
(5n)
Vertical coordinate z (m)
Cross-stream coordinate n (m)
Left bank
(outer)
+ n
Centerline
(n = 0)
- n
Right bank
(inner)

**Figure 4**

depths $h$ from the initial run with constant flow to calculate local drag coefficients from the following relation:

$$C_d = \left[\frac{1}{h}\int_{z_0}^{h} f(z, z_0)dz\right]^{-2} \tag{2}$$

The integrand is a function that describes the vertical structure of the flow, in this case given by the logarithmic law of the wall:

$$f(z, z_0) = \frac{\mathbf{u}}{u*} = \frac{1}{k}\ln\left(\frac{z}{z_0}\right) \tag{3}$$

where $\mathbf{u}$ is the velocity at a height $z$ above the bed, $u*$ is the shear velocity, and $k$ is Von Karman's constant, equal to 0.408. Flow resistance parameterization is discussed in greater detail by *Lisle et al.* [2000], who found that FaSTMECH was not particularly sensitive to the method used to specify drag coefficients. In this study, all analyses of the local force balance were based on the latter set of model runs with depth-dependent, spatially variable flow resistance.

### 2.3. Force Balance Analysis

[27] For each of the four time periods and three discharges considered in this study, the numerical flow model provided spatially distributed predictions of depth, velocity, water surface elevation, and boundary shear stress. We used these results to decompose FaSTMECH output into the individual forces governing the flow field. Each of these forces corresponds to a specific term in an equation expressing conservation of fluid momentum. Cast in an orthogonal curvilinear coordinate system defined by a streamwise axis $s$ oriented along the channel centerline, a cross-stream (normal) axis $n$, and a nearly vertical $z$ axis oriented perpendicular to the bed (Figure 4), the $s$ and $n$ components of this momentum equation are given by [*Nelson and Smith*, 1989a]

$$\underbrace{\frac{1}{(1-N)}\frac{\partial}{\partial s}\left(\langle u\rangle^2 h\right)}_{1_s} + \underbrace{\frac{\partial}{\partial n}(\langle u\rangle\langle v\rangle h)}_{2_s} - \underbrace{2\frac{\langle u\rangle\langle v\rangle h}{(1-N)R}}_{3_s} = \underbrace{-\frac{gh}{(1-N)}\frac{\partial E}{\partial s}}_{4_s} - \underbrace{\frac{1}{\rho}(\tau_{zs})_B}_{5_s} + \varepsilon_s \tag{4}$$

and

$$\underbrace{\frac{1}{(1-N)}\frac{\partial}{\partial s}(\langle u\rangle\langle v\rangle h)}_{1_n} + \underbrace{\frac{\partial}{\partial n}\left(\langle v\rangle^2 h\right)}_{2_n} - \underbrace{\frac{\left(\langle u\rangle^2 + \langle v\rangle^2\right)h}{(1-N)R}}_{3_n} = \underbrace{-gh\frac{\partial E}{\partial n}}_{4_n} - \underbrace{\frac{1}{\rho}(\tau_{zn})_B}_{5_n} + \varepsilon_n \tag{5}$$

The variables appearing in expressions (4) and (5) are defined in Table 4, and sign conventions are illustrated in Figure 4. Equations (4) and (5) are arranged with spatial gradients in velocity (i.e., spatial accelerations; the flow is assumed to be steady in time) on the left and forces on the right. Each term has dimensions of [$L^2$ $T^{-2}$], equivalent to a force per unit area, denoted by $\tau$, for a control volume of fluid of density $\rho$; in that sense, these expressions describe the local force balance. The individual components of this balance are listed in Table 5 and illustrated, in a conceptual manner, in Figure 4. Simplified models of bend flow involve a balance between the downstream pressure gradient ($4_s$), the streamwise component of the boundary shear stress ($5_s$), the centrifugal force due to channel curvature ($3_n$), and the cross-stream pressure gradient ($4_n$), but disregard the so-called topographic steering effects represented by the terms labeled $1_s$, $2_s$, $1_n$ and $2_n$ [*Dietrich*, 1987]. In this study, we sought a more complete understanding of the local force balance by considering all of the terms in equations (4) and (5). We were particularly interested in the manner in which point bar development leads to topographically induced convective accelerations ($1_s$, $2_s$, $1_n$, and $2_n$) and thus influences the other components of the local force balance.

[28] The information required to evaluate individual force balance components was provided as output from FaSTMECH. This analysis made use of the following quantities: the $s$ and $n$ coordinates of the model grid nodes; radius of curvature values for the centerline digitized to define the computational grid; and model predictions of $\langle u\rangle$, $\langle v\rangle$, $h$, $E$, $(\tau_{zs})_B$, and $(\tau_{zn})_B$. For each location within the channel, these data were used to calculate each of the terms listed in Table 5. For example, spatially distributed values of $1_s$, representing the change in streamwise momentum along the channel, were obtained by (1) squaring the predicted value of $\langle u\rangle$ for every element of the model grid; (2) multiplying the resulting $\langle u\rangle^2$ values element-by-element with the collocated grid of $h$ predictions to yield a grid composed of values of the quantity $(\langle u\rangle^2 h)$; (3) computing the streamwise partial derivative of $(\langle u\rangle^2 h)$ as centered finite differences for interior grid points and forward differences for points along the edges of the model domain; and (4) performing another element-by-element multiplication of the resulting grid of $\partial/\partial s(\langle u\rangle^2 h)$ values with a collocated grid of $1/(1-N)$ values derived from grids of $n$ coordinates and $R$ values.

[29] The other terms were computed using analogous procedures. These calculations allowed us to quantify, for each time period and discharge considered, the individual components of the local force balance. Because this analysis was based on spatially distributed model output, plan view maps and cross sections of the various terms illustrated the magnitude and spatial pattern of the forces governing the flow field.

## 3. Results

### 3.1. Morphologic Adjustments

[30] Morphologic evolution of the Robinson Reach from a relatively featureless, engineered river toward a more complex, alluvial state is illustrated in Figure 5. The initial

**Figure 4.** (a) Conceptual diagram of the channel-centered coordinate system (plan view) and (b) force balance components in profile and (c) in cross section. The numbers correspond to the terms listed in Table 5, and the arrows indicate the direction(s) in which each force acts; double-headed arrows imply that the force could be exerted in either direction. The circled dots and circled crosses represent directions out of and into the plane of the page, respectively.

**Table 4.** Definitions of Variables in the Streamwise and Cross-Stream Momentum Equations (4) and (5)[a]

| Symbol | Variable | Description |
|---|---|---|
| $s$ | Streamwise coordinate | Increases downstream |
| $n$ | Cross-stream coordinate | $n = 0$ at the centerline and takes on larger positive (negative) values toward the left (right) bank |
| $z$ | Vertical coordinate | $z = 0$ at the bed and increases upward, perpendicular to the channel boundary |
| $R$ | Centerline radius of curvature | $R$ is positive (negative) where the channel curves to the left (right), looking downstream |
| $\langle u \rangle$ | Streamwise component of vertically averaged velocity vector | Positive downstream |
| $\langle v \rangle$ | Cross-stream component of vertically averaged velocity vector | Positive (negative) toward left (right) bank |
| $h$ | Flow depth | |
| $1 - N = 1 - n/R$ | Downstream metric coefficient for channel-centered coordinate system | Accounts for differences in path length with transverse position [*Smith and McLean*, 1984] |
| $g$ | Acceleration due to gravity | |
| $E$ | Water surface elevation | |
| $\rho$ | Fluid density | |
| $(\tau_{zs})_B$ | Streamwise component of boundary shear stress vector | Positive downstream |
| $(\tau_{zn})_B$ | Cross-stream component of boundary shear stress vector | Positive (negative) toward left (right) bank |
| $\varepsilon_s$ | Residual term for streamwise momentum equation | Represents effects excluded from this formulation |
| $\varepsilon_n$ | Residual term for cross-stream momentum equation | Represents effects excluded from this formulation |

[a]The residual terms $\varepsilon_s$ and $\varepsilon_n$ represent higher-order effects, such as lateral stresses, not included in this formulation; for a thorough derivation and scaling arguments, see *Nelson and Smith* [1989b].

design of the reconstructed channel consisted of meander bends with wide, flat-bottomed pools separated by long, straight, and slightly narrower riffle sections. The constructed channel bends had approximately planar cross-stream bed slopes that extended only a small portion of the distance across the channel but were steeper than would be predicted by method of *Ikeda* [1989], which balances the outward gravitational force acting on sediment grains against the inward directed shear stress due to curvature-induced secondary circulation; models of this kind neglect topographic steering effects. In addition, the original channel design superimposed deepened pools onto the longitudinal profile of the bed. For these reasons, the initial configuration of the Robinson Reach did not exactly conform to an equilibrium bend of the kind conceptualized by *Ikeda* [1989] and others [e.g., *Johannesson and Parker*, 1989]. Although no sustained, high-magnitude flows occurred between the end of construction in February 2002 and our March 2005 survey, the elevation difference map in Figure 5a indicates that bed material was mobile during this period and had begun to accumulate to depths of up to 1 m on the inner bank near the entrance to each bend. Small amounts of erosion occurred along the outer bank of each bend downstream of the apex, on the left side of the channel upstream of the first bend, and in an elongated swath through the riffle.

[31] Morphologic response to the 2005 flood was much more pronounced, and comparing surveys from before and after this event revealed clear patterns of topographic adjustment (Figure 5b). Large volumes of sediment were deposited along the inner bank of each meander, locally exceeding 1 m in thickness. Relative to their apices, deposition occurred farther downstream in the first bend than in the second, due to the larger amount of bed material that had accumulated at the upstream end of the first bend prior to the 2005 flood event; this incipient deposit developed into a well-defined point bar. In the second bend, a similar bar formed but had a lower amplitude and did not extend as far toward the inner bank. The deposition zone on the right side of the channel upstream of the first bend represents the downstream extent of a large bar that developed where the channel abruptly changes direction to enter the engineered portion of the Robinson Reach. Bank erosion opposite this bar resulted in over 1 m of scour on the left side of the channel at the upstream end of our study area. Similar depths of scour were observed in narrow, elongated zones along the outer bank of both bends, with lesser erosion extending into the riffles.

**Table 5.** Terms in the Streamwise and Cross-Stream Momentum Equations (4) and (5), Using the Variables Defined in Table 4[a]

| Term | Expression | Description |
|---|---|---|
| $1_s$ | $\frac{1}{(1-N)}\frac{\partial}{\partial s}(\langle u \rangle^2 h)$ | Change in streamwise fluid momentum along the channel |
| $2_s$ | $\frac{\partial}{\partial n}(\langle u \rangle\ \langle v \rangle\ h)$ | Change in streamwise fluid momentum across the channel |
| $3_s$ | $-2\frac{\langle u \rangle \langle v \rangle h}{(1-N)R}$ | Centrifugal acceleration of flow due to channel curvature |
| $4_s$ | $-\frac{gh}{(1-N)}\frac{\partial E}{\partial s}$ | Streamwise pressure gradient force |
| $5_s$ | $-\frac{1}{\rho}(\tau_{zs})_B$ | Streamwise component of boundary shear stress |
| $1_n$ | $\frac{1}{(1-N)}\frac{\partial}{\partial s}(\langle u \rangle\ \langle v \rangle\ h)$ | Change in cross-stream fluid momentum along the channel |
| $2_n$ | $\frac{\partial}{\partial n}(\langle v \rangle^2 h)$ | Change in cross-stream fluid momentum across the channel |
| $3_n$ | $-\frac{(\langle u \rangle^2 + \langle v \rangle^2)h}{(1-N)R}$ | Centrifugal acceleration of flow due to channel curvature |
| $4_n$ | $-gh\frac{\partial E}{\partial n}$ | Cross-stream pressure gradient force |
| $5_n$ | $-\frac{1}{\rho}(\tau_{zn})_B$ | Cross-stream component of boundary shear stress |

[a]These forces are illustrated conceptually in Figure 4. The terms labeled $1_s$, $2_s$, $1_n$, and $2_n$ represent spatial gradients in velocity due steering of the flow by morphologic features such as point bars and are thus referred to as topographically induced convective accelerations. The shear stress terms $5_s$ and $5_n$ represent the effects of frictional forces exerted along the channel boundary and account for turbulent diffusion of momentum from the interior of the flow to the low momentum region near the bed. The pressure gradient terms $4_s$ and $4_n$ account for the along-channel water surface slope and cross-stream tilt (superelevation) of the water surface, respectively.

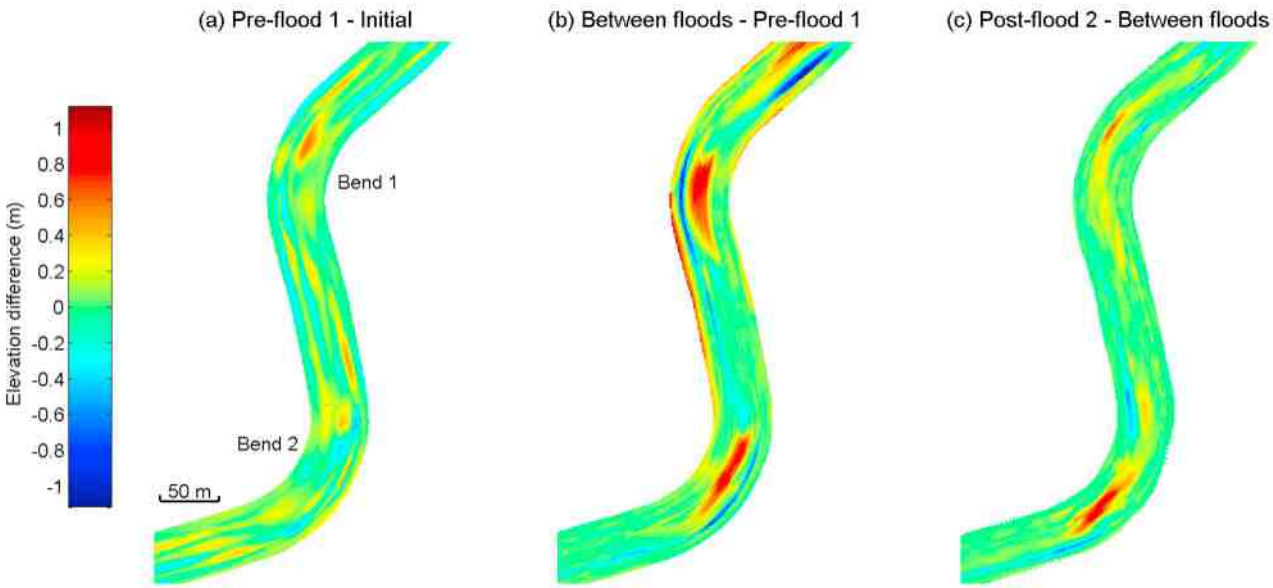


**Figure 5.** Morphologic evolution observed along the Robinson Reach of the Merced River. Changes in bed elevation that occurred (a) between the initial, as-built channel configuration and a survey conducted immediately prior to the first flood; (b) during the first flood event; and (c) in 2006 as a result of the second flood event are illustrated. The two bends examined in this study are labeled in Figure 5a.

[32] Despite its higher peak discharge and longer duration, the 2006 flood produced a smaller morphologic response. This observation suggests that the adjustments that occurred during the first flood established a more stable channel geometry, and/or that a lower sediment supply during the second event was not sufficient to support a similar degree of bar growth. Nevertheless, Figure 5c indicates that deposition occurred on the upstream margin of the first point bar and that the second bar grew downstream and began to wrap around the second bend. Erosion along the first bend was relatively minor, but for the second bend erosion of the outer bank continued and progressed downstream well past the bend apex, implying a downstream component of meander migration. In general, the morphologic changes observed along the Robinson Reach, primarily the development of point bars along the inside of each bend and erosion of the outer banks, were consistent with geomorphic theory regarding flow and sediment transport in meandering channels [e.g., *Dietrich*, 1987].

[33] The hydrograph shown in Figure 2 indicates that the morphologic changes illustrated in Figure 5 primarily occurred during two periods of sustained overbank flooding, whereas in-bank flows prior to March 2005 had relatively little impact on the topography. In this study, we did not attempt to model flow conditions during the flood events due to a lack of topographic data for the floodplain and the difficulty of adapting our numerical model for this purpose. During the 2005 flood, we observed that flow depths across the broad, low-relief floodplain were on the order of 20–30 cm, implying that even for discharges three times greater than bankfull, increases in stage were relatively minor. In any case, a detailed examination of overbank flow patterns during these floods was beyond the scope of the current investigation, which focused on in-channel flows for discharges up to bankfull. We acknowledge, however, that the sequence of channel configurations upon which our force balance analyses were based might have been shaped by overbank flows that differed in important ways from the bankfull and subbankfull flows we simulated [e.g., *Wormleaton et al.*, 2005; *Shiono et al.*, 2009a, 2009b]. Because we made no attempt to model morphologic evolution, we simply used the measured topography for each time period to examine in-bank flows for each channel configuration, taking as given any influence overbank flood events might have had on that particular geometry.

### 3.2. Flow Model Calibration and Verification

[34] Calibrating flow resistance for the FaSTMECH hydraulic model involved comparing predicted water surface elevations to surveyed profiles. Because these water surface data were collected following the second flood event, model runs based on the November 2006 topography were used to perform the calibration. Initially, the drag coefficient was assumed spatially uniform and a numerical procedure used to adjust the value of $C_d$ to minimize the discrepancy between predicted and observed water surface elevations. The results of this calibration are summarized in Table 6, which indicates that $C_d$ was inversely related to discharge. These $C_d$ values were used for the earlier time periods as well. As described in section 2.2, we used output from the initial set of runs with a uniform $C_d$ to perform a second round of modeling in which flow resistance was allowed to vary spatially as a function of the local flow depth, which produced a small improvement in the water surface elevation RMSE (Table 6). We also assessed model performance by examining predicted and observed water surface profiles and residual maps (Figure 6) which indicated some slight but systematic discrepancies. Relative to the surveyed profiles, the model tended to smooth out streamwise variations in water surface slope, with gradients

**Table 6.** FaSTMECH Model Calibration and Water Surface Elevation Verification for the Three Discharges $Q$ for Which Surveyed Profiles Were Available[a]

| $Q$ ($m^3/s$) | $C_d$ | $LEV$ ($m^2/s$) | Constant $C_d$ WSE RMSE (m) | Variable $C_d$ WSE RMSE (m) |
|---|---|---|---|---|
| 42.5 | 0.0101 | 0.0122 | 0.045 | 0.042 |
| 32.6 | 0.0118 | 0.0101 | 0.044 | 0.028 |
| 6.4 | 0.0170 | 0.0030 | 0.033 | 0.033 |

[a]Disagreement between predicted and observed water surface elevations (WSE) is summarized in terms of the root mean square error (RMSE). The initial drag coefficient values were calibrated assuming that $C_d$ was spatially uniform, but force balance analysis was based on a second set of runs in which $C_d$ varied spatially, as described in section 2.2.

overpredicted (underpredicted) through pools (riffles). We tentatively attribute this error to a restoration design in which the curved sections (i.e., pools) were wider than the intervening straight segments (i.e., riffles). The resulting, fairly abrupt increase (decrease) in width at the entrance to (exit from) each bend might not have been represented accurately in the gridded topography used as input to the flow model, which in turn produced water surface profiles that were smoother than the field data. Nevertheless, overall agreement between modeled and measured elevations was close, with RMS errors ranging from 0.028 to 0.042 m.

[35] Field measurements of flow velocity, described in section 2.1, were also used to assess the accuracy of model predictions and evaluate our parameterization of flow resistance. Allowing the drag coefficient to vary spatially as a function of local depth via equations (2) and (3) resulted in higher values of $C_d$ and hence lower velocities in shallower areas and vice versa where the flow was deeper. Figure 7 compares depth-averaged velocity magnitudes, denoted by $\langle \mathbf{u} \rangle$, predicted with both constant and spatially variable (depth-dependent) drag coefficients to data acquired under base flow conditions (6.4 $m^3/s$) with the SonTek FlowTracker ADV. When $C_d$ was held constant, the model tended to homogenize the flow field relative to our observations, with overprediction of low velocities and underprediction of high velocities, particularly for more asymmetric pool cross sections (Figures 7b, 7d, and 7f). This effect was mitigated by allowing $C_d$ to vary spatially as a function of depth via the approach described in section 2.2. The latter set of model runs produced higher predicted velocities in the thalweg and lower velocities near the banks that more closely matched the field data, most notably for

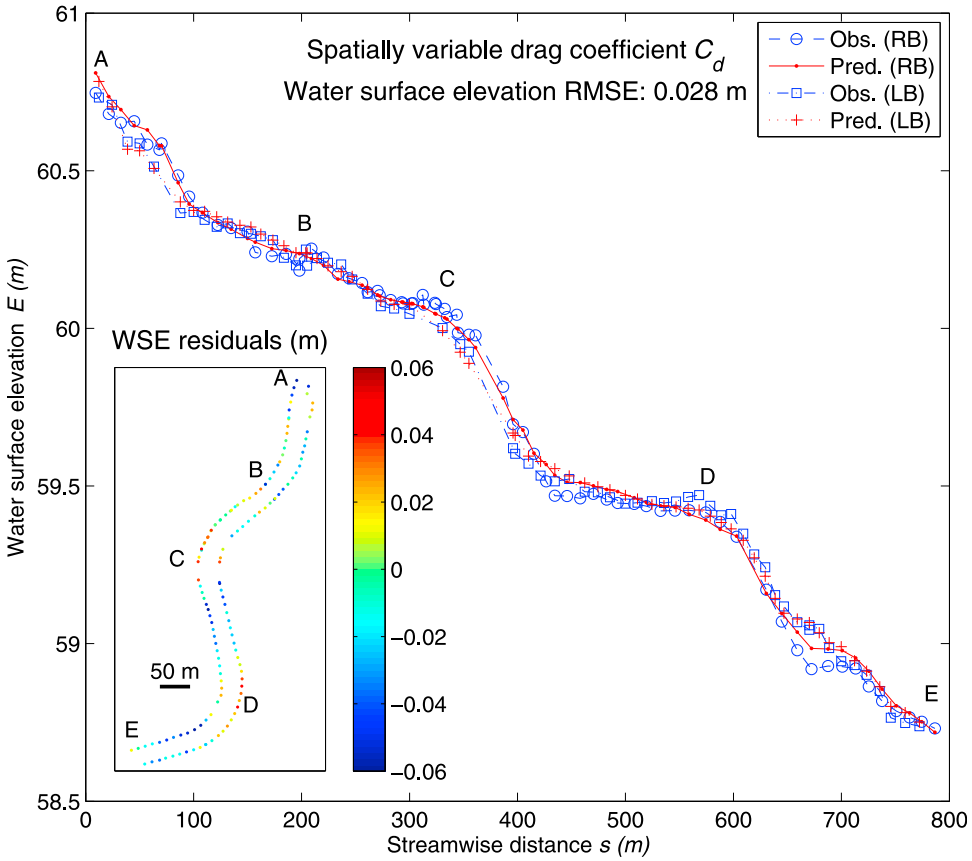


**Figure 6.** Water surface elevation verification for a modeled discharge of 32.6 $m^3/s$, the post-flood 2 topography, and a spatially variable drag coefficient $C_d$. Predicted and observed water surface elevations are plotted as longitudinal profiles, and the right and left banks are distinguished from one another. The inset is a map of water surface elevation residuals, defined as observed predicted. Text labels indicate the same locations in map view and along the profile, with bend 1 located at C and bend 2 located at D. The corresponding water surface elevation root mean square error (RMSE) is also indicated. Similar profiles and maps were produced for the other modeled discharges as well (Table 6).

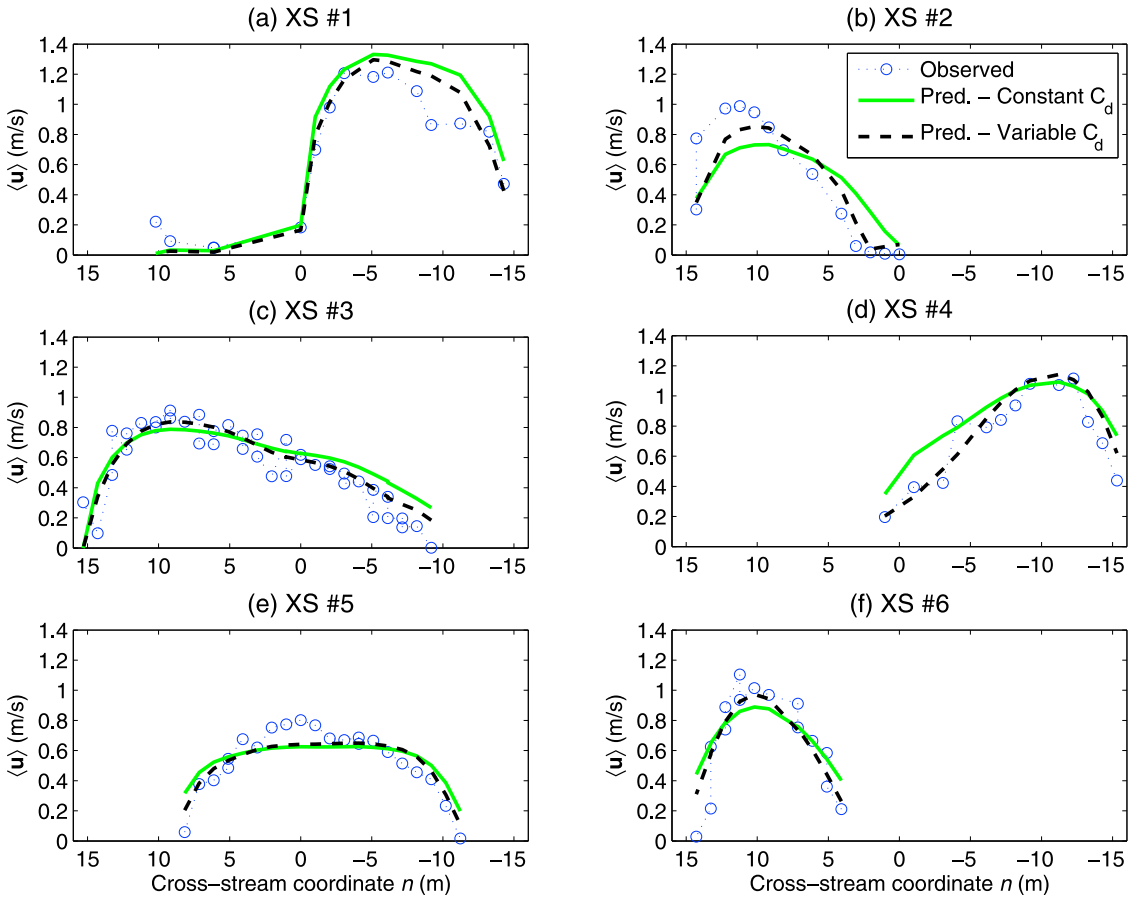


**Figure 7.** Comparison of predicted and observed depth-averaged velocity magnitudes, denoted by $\langle \mathbf{u} \rangle$, at a discharge of 6.4 $m^3/s$ for FaSTMECH model runs (based on the post-flood 2 topography) with a single, spatially constant drag coefficient $C_d$ and with spatially variable drag coefficients. Velocity measurements were obtained in November 2006, during the post-flood 2 time period after the bars had developed. View is downstream and the location of each transect is indicated in Figure 1.

cross sections 2 and 4 (Figures 7b and 7d). The regression analyses summarized in Table 7 indicated a strong overall agreement between predicted and observed velocities and confirmed that a spatial variable parameterization of flow resistance produced an improvement over the uniform $C_d$ model runs in terms of both regression $R^2$ values and predicted versus observed RMS errors. We thus used FaSTMECH runs with spatially variable drag coefficients to characterize hydraulic adjustments and quantify force balance components.

[36] Model performance under high-flow conditions was assessed using velocity data recorded by a SonTek ADP at a discharge of 42.5 $m^3/s$. The results of this comparison are summarized in Figure 8 and Table 8, which indicate good agreement between predicted and observed depth-averaged velocity magnitudes at an approximately bankfull flow. For ADP transects A and B, the model appeared to systematically overpredict $\langle \mathbf{u} \rangle$ relative to the field measurements in shallow flow over the bars located on the right and left side of the channel, respectively. At least a portion of this discrepancy was a consequence of the manner in which the ADP data were collected and processed. Because the instrument had a total blanking distance of 0.3 m, velocity information was not available for the uppermost portion of the water column. For shallow flow over the bars, the ADP thus recorded data for a smaller number of vertical cells located closer to the channel boundary, where velocities were lower due to friction along the bottom. Averaging the velocity magnitudes for these near-bed cells thus produced a negatively biased estimate of $\langle \mathbf{u} \rangle$, whereas the depth-averaged velocities predicted by the model considered the full flow depth and thus produced larger values of $\langle \mathbf{u} \rangle$. In deeper portions of the channel, the ADP sampled a greater number of cells encompassing a larger proportion of the depth

**Table 7.** Verification of FaSTMECH Predictions of Flow Velocity[a]

| $C_d$ | $b_1$ | $b_0$ (m/s) | $R^2$ | ⟨u⟩ RMSE (m/s) |
|---|---|---|---|---|
| Uniform | 0.98 | −0.039 | 0.74 | 0.16 |
| Spatially variable | 0.97 | 0.0015 | 0.85 | 0.12 |

[a]Regression analyses ($n$ = 118) were used to compare field measurements to predicted velocity magnitudes for model runs with uniform and spatially variable drag coefficients. Linear regression equations were of the form $\langle \mathbf{u}_{obs} \rangle = b_0 + b_1 \langle \mathbf{u}_{pred} \rangle$. The summary statistics listed are the coefficient of determination $R^2$ and root mean square error (RMSE) between predicted and observed velocities; the mean of the measured velocities was 0.59 m/s.

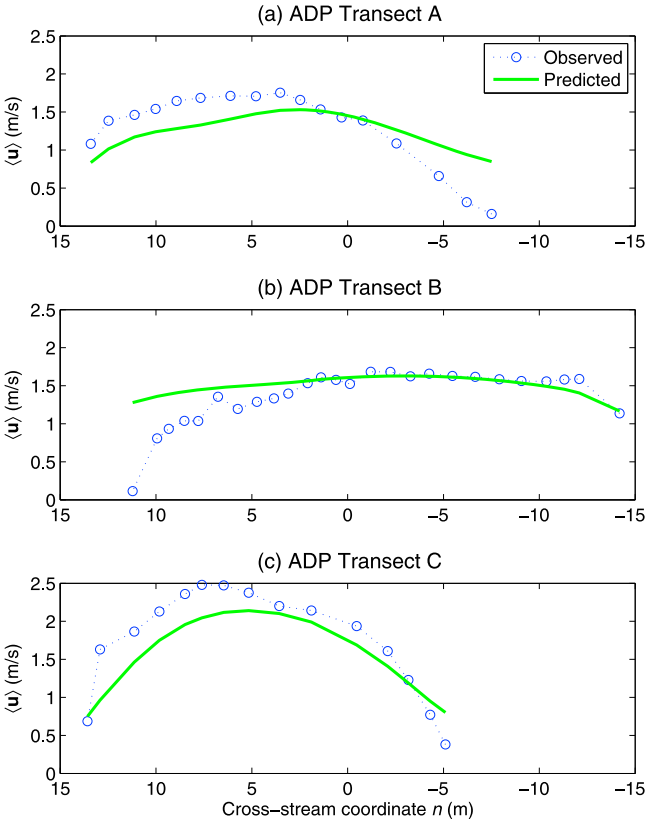


**Figure 8.** Comparison of predicted (from FaSTMECH output) and observed (ADP measurements) depth-averaged velocity magnitudes, denoted by $\langle \mathbf{u} \rangle$, at a discharge of 42.5 $m^3/s$ for the post-flood 2 topography measured after the bars had developed. View is downstream, and the location of each transect is indicated in Figure 1.

and agreement between observed and predicted values of $\langle \mathbf{u} \rangle$ were much better. Removing shallow ADP profiles consisting of three or fewer vertical cells from the data set improved the predicted versus observed regression $R^2$ from 0.65 to 0.74. The RMS errors of 0.31 m/s and 0.27 m/s for the full data set and the subset for which shallow points were excluded were 22% and 18% of the mean of the measured values of $\langle \mathbf{u} \rangle$, respectively. These results imply that the FaSTMECH numerical model produced reliable simulations of the velocity field at a bankfull discharge and thus provide some justification for our use of model output to examine the force balance at a flow of morphogenetic significance.

[37] To assess the model's sensitivity to grid resolution, we performed a basic grid convergence analysis following the procedure described by *Hardy et al.* [2003]. Based on the same set of initial centerline vertices used to generate the original grid (1.02 m spacing between nodes), we produced additional grids with approximately twice the number of nodes and half the number of nodes (Table 9). Model runs for a bankfull discharge of 42.5 $m^3/s$ were performed for each of these new grids, with the post-flood 2 topography used as input, and the resulting predictions of water surface elevation, depth, and streamwise and cross-stream velocity components compared to predictions derived from the original grid. Because FaSTMECH requires that the number of streamwise and cross-stream nodes be odd, we could not exactly double and halve the original resolution, and the nodes of the increased- and reduced-resolution grids did not coincide precisely with the nodes of the original grid. To overcome this slight geometric inconvenience, we used a simple linear interpolation to determine modeled values of $E$, $h$, $\langle u \rangle$, and $\langle v \rangle$ at the nodes of the coarser-resolution grid from the flow solutions for the finer-resolution grid. The resulting set of coincident predictions were then used to compute RMS errors for each hydraulic variable (Table 9). For the original and half resolution grids, RMS errors for $E$, $h$, and $\langle u \rangle$ were less than 3% of the mean values for each quantity, but the RMS error for $\langle v \rangle$ was 30% of the reach-averaged absolute value of the cross-stream velocity. Comparison of the original- and double-resolution grids was problematic because the 0.5 m node spacing of the higher-resolution grid proved computationally demanding and we had to limit the number of model iterations in order to converge on a flow solution. A comparison of the FaSTMECH output for these two grids indicated that predictions of $E$ and $h$ were fairly robust but that RMS errors for the two velocity components were larger. In general, a related study also conducted on the Merced River found that the most important input to the flow model, regardless of grid resolution, was the bed topography [*Legleiter et al.*, 2011], and the density of our survey data was not sufficient to support the higher-resolution grid. The 1.02 m grid spacing employed here thus represented a compromise between the available topographic data and computational resources and an adequate representation of cross-stream velocities.

### 3.3. Changes in Bankfull Hydraulics

[38] Before considering the force balance in detail, we first examined changes in the flow field over time for the two meander bends indicated in Figure 1. We focused on these two bends because they had a simple, consistent planform geometry and were located well downstream of the entrance to the engineered portion of the Robinson Reach, where abrupt changes in channel direction and bed slope created more complicated conditions. The streamwise extent of each bend was defined by computing the centerline curvature and determining where the curvature series crossed zero in the straight segments between bends. Figure 9 illustrates measured changes in bed topography and modeled adjustments of the water surface, velocity, and boundary shear stress fields for the central portion of bend 1 at an approximately bankfull discharge of 42.5 $m^3/s$. Each column corresponds to one of the surveys indicated in Figure 2, and these maps thus summarize the morphologic

**Table 8.** Verification of FaSTMECH Predictions of Flow Velocity[a]

| Data Set | $b_1$ | $b_0$ (m/s) | $R^2$ | ⟨u⟩ RMSE (m/s) |
|---|---|---|---|---|
| All profiles ($n$ = 58) | 1.32 | −0.46 | 0.65 | 0.31 |
| Shallow excluded ($n$ = 41) | 1.34 | −0.41 | 0.74 | 0.27 |

[a]Regression analyses were used to compare field measurements obtained with an ADP at a discharge of 42.5 $m^3/s$ to predicted velocity magnitudes. Linear regression equations were of the form $\langle \mathbf{u}_{obs} \rangle = b_0 + b_1 \langle \mathbf{u}_{pred} \rangle$. The summary statistics listed are the coefficient of determination $R^2$ and root mean square error (RMSE) between predicted and observed velocities. The mean of the measured depth-averaged velocities was 1.45 m/s for all of the profiles and 1.57 m/s when shallow locations were excluded.

**Table 9.** Grid Convergence Analysis for FaSTMECH Numerical Flow Model Runs Based on the Post-Flood 2 Topography and a Bankfull Discharge of 42.5 $m^3/s$[a]

| Grid | Dimensions ($N_s \times N_n$) | Node Spacing ($\Delta s$, $\Delta n$) (m) | $E$ (m) | $h$ (m) | $\langle u \rangle$ (m/s) | $\langle u \rangle$ (m/s) |
|---|---|---|---|---|---|---|
| Half | 389 × 25 | 2.045, 2.125 | 0.019 | 0.021 | 0.070 | 0.024 |
| Original | 779 × 51 | 1.020, 1.020 | | | | |
| Original | 779 × 51 | 1.020, 1.020 | 0.032 | 0.033 | 0.169 | 0.098 |
| Double | 1559 × 103 | 0.509, 0.500 | | | | |

[a]Model predictions of the indicated hydraulic quantities are compared for each pair of grids at the locations of the nodes of the coarser-resolution grid and used to compute the root mean square error values reported.

and hydraulic condition of the simple, engineered channel and the river's response to two periods of sustained overbank flooding. The patterns observed in the two bends were quite similar, and the following description of the hydraulic changes that occurred in bend 1 also pertains to bend 2.

[39] The topographic time series depicted in Figure 9a highlights the formation and growth of a large point bar along the convex bank, along with significant overall aggradation. The initial, wide, flat-bottomed pool acted as an effective sediment trap, particularly during the first flood. The more subdued topographic response to the second event suggests that by this time, most of this accommodation space had been occupied by bed material that entered the reach during the 2005 flood. Initially, the water surface gradient was steepest over the riffle upstream of bend 1 and much gentler through the center of the meander (Figure 9b). Aggradation near the bend entrance produced a minor increase in slope approaching the apex prior to the first flood, but point bar deposition during this event reduced the

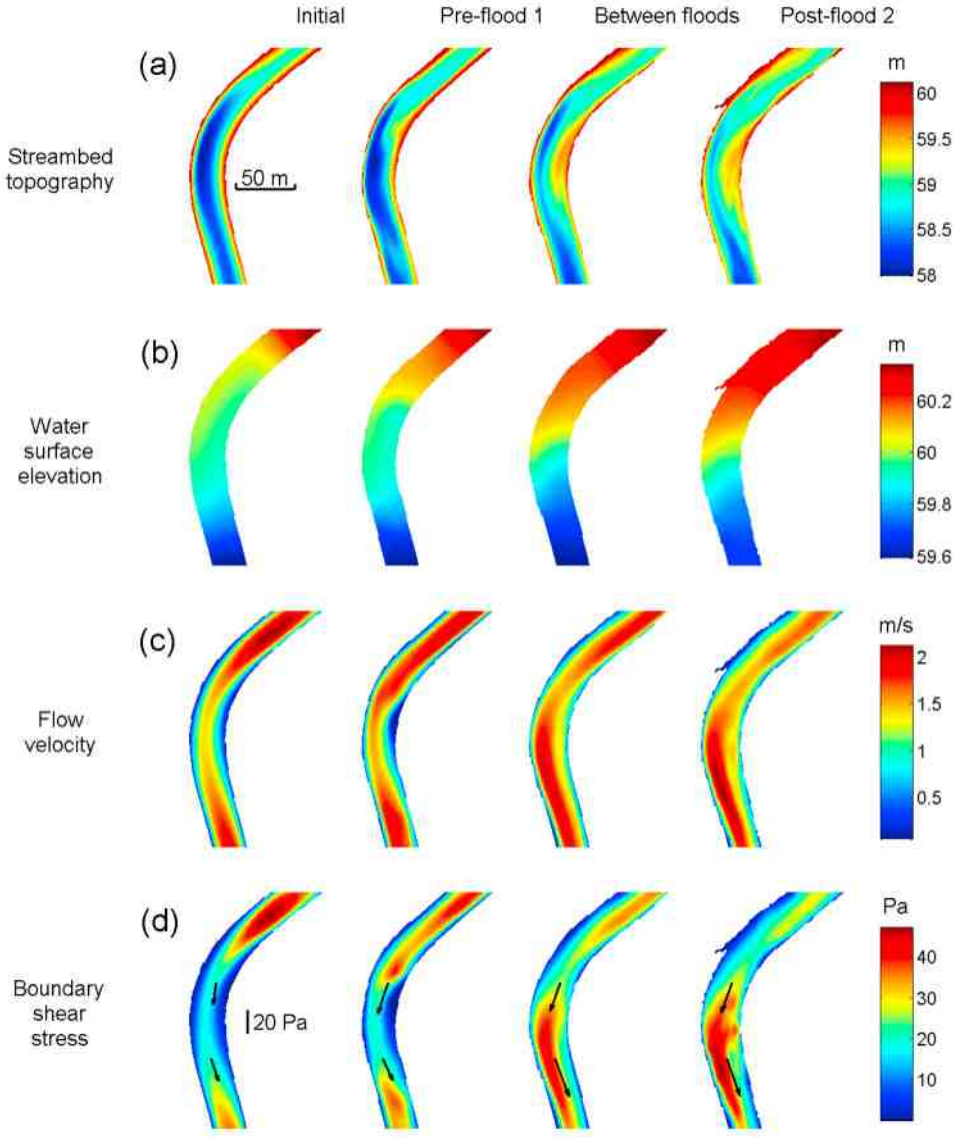


**Figure 9.** Comparison of (a) bed topography, (b) water surface elevation, (c) flow velocity, and (d) boundary shear stress over time for bend 1 of the Robinson Reach of the Merced River. Each column corresponds to one of the time periods indicated in Figure 2. The boundary shear stress vectors along the channel centerline upstream and downstream of the bend apex are indicated in Figure 9d.

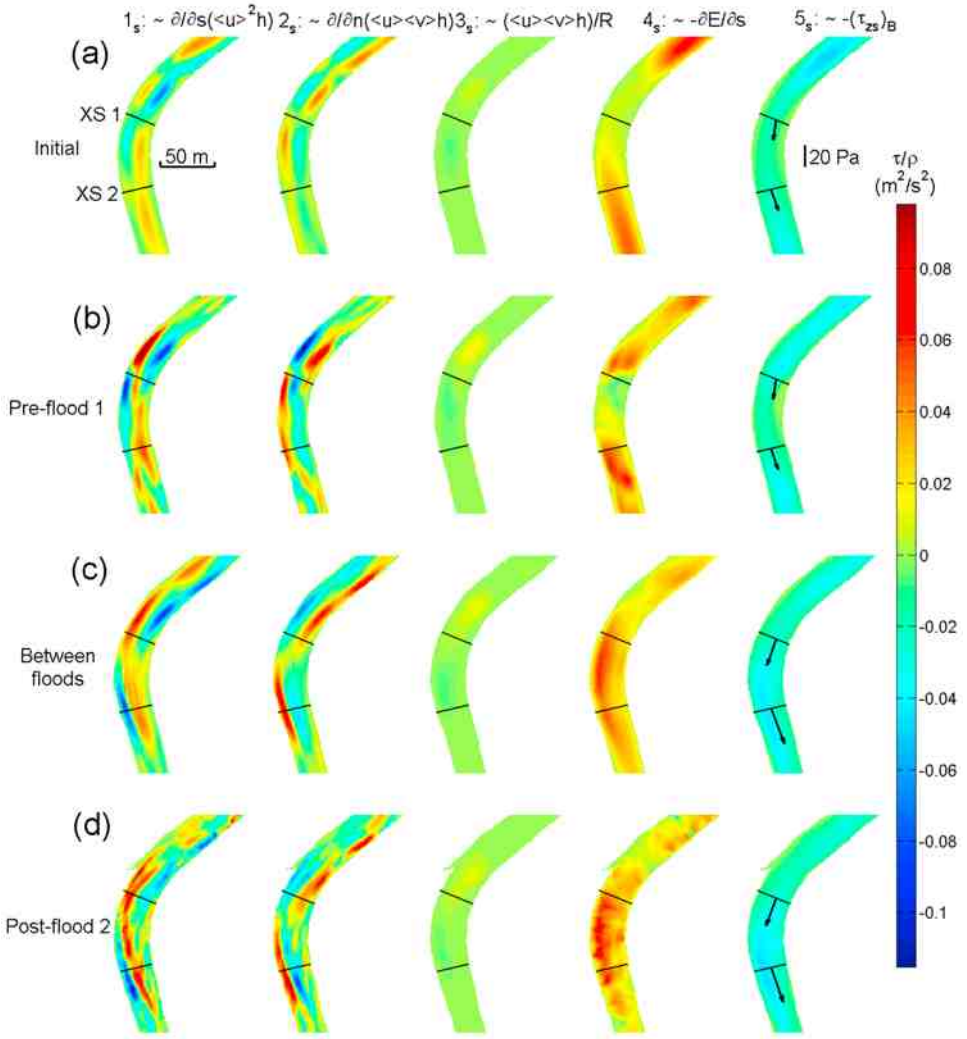


**Figure 10.** Comparison of streamwise force balance components over time for bend 1 at an approximately bankfull discharge. (a-d) Same as the time periods indicated in Figure 2. Columns represent terms in the momentum equation. Due to lack of space, the heading for each column includes only the most critical quantity in each term, but the plotted data represent values of the entire term as specified in equation (4). The boundary shear stress vectors along the channel centerline upstream and downstream of the bend apex are indicated in each row of the fifth column. The locations of the cross sections depicted in Figures 12, 15, and 16 are also shown.

cross-sectional area of the flow and resulted in a general increase in both the along- and across-stream water surface gradients through the upstream half of the bend. These patterns were amplified only slightly by the second flood event. Adjustments of the velocity field tracked the changes in water surface elevation (Figure 9c). For the initial channel design, velocities were greatest entering and exiting the bend and approximately 25% lower through the apex. By the time of our pre-flood 1 survey, a zone of greater velocities connecting the riffles was evident, but a well-developed high-velocity core did not form until after the first flood. By October 2005, velocities were reduced in the upstream portion of the bend but increased significantly along the outer bank beginning near the apex, where expansion of the bar acted to concentrate the flow toward the right side of the channel. Following the second flood event, velocities near the bend entrance decreased further while the high-velocity core became stronger and shifted slightly downstream. The boundary shear stress field exhibited a similar response to the two floods (Figure 9d). For the initial and pre-flood 1 channel configurations, $\tau_B$ was greatest in the riffle upstream of bend 1, with much lower values through the bend. Bar growth during the two flood events reduced $\tau_B$ in the upstream portion of the bend, but constriction of the flow by the bar resulted in much greater stresses at and downstream of the bend apex, particularly near the right bank where velocities were greatest. Upstream of the apex, the orientation of the shear stress vector along the channel centerline shifted toward the outer bank as the bar grew.

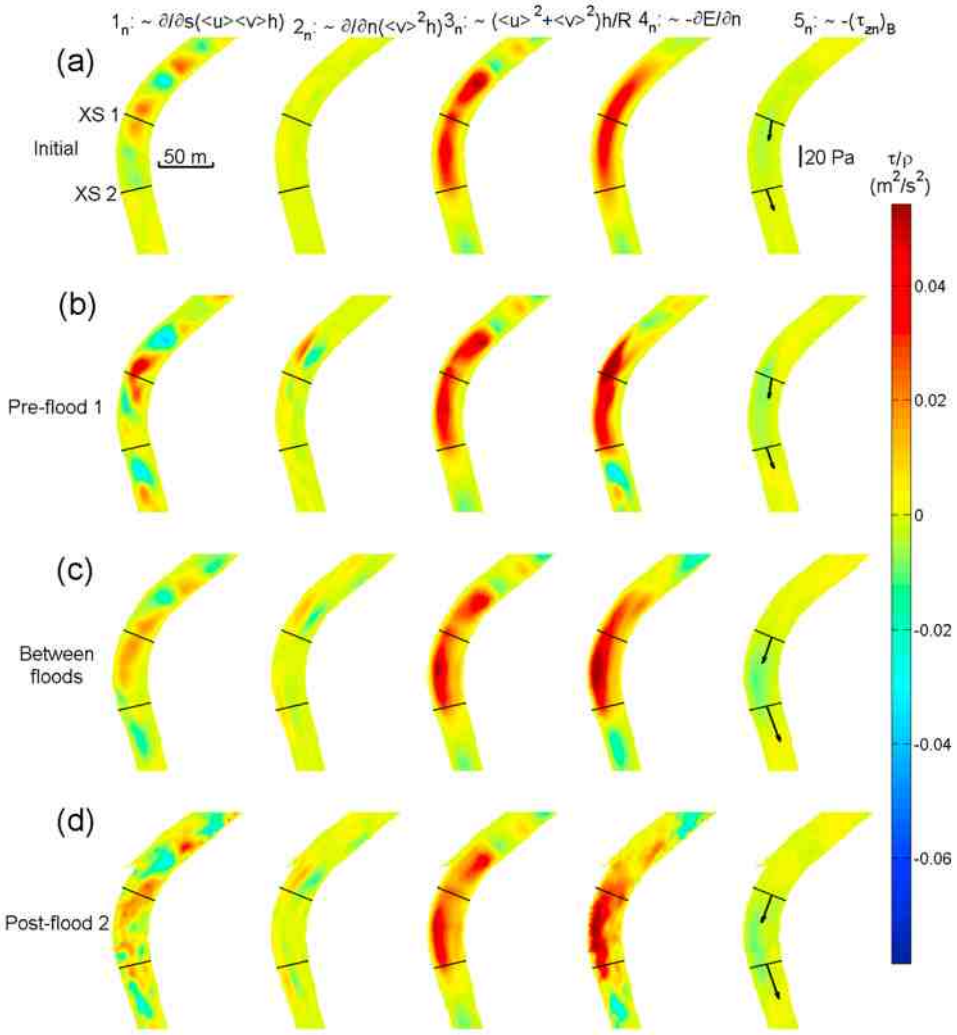


**Figure 11.** Comparison of cross-stream force balance components over time for bend 1 at an approximately bankfull discharge. (a-d) Same as the time periods indicated in Figure 2. Columns represent terms in the momentum equation. Due to lack of space, the heading for each column includes only the most critical quantity in each term, but the plotted data represent values of the entire term as specified in equation (5). The boundary shear stress vectors along the channel centerline upstream and downstream of the bend apex are indicated in the fifth column. The locations of the cross sections plotted in Figures 12, 15, and 16 are also shown.

### 3.4. Adjustments of the Local Force Balance

[40] In this section, we decompose and interpret these hydraulic changes by examining the adjustments of the local force balance that occurred over time. Individual terms in the momentum equations were evaluated as described in section 2.3, and results for bend 1 were summarized using maps (Figures 10 and 11), in which each column represents one of the terms listed in Table 5 and each row corresponds to one of our survey data sets, and cross sections (Figure 12). Sections 3.4.1–3.4.4 describe results from each time period in turn.

#### 3.4.1. Initial Channel Configuration

[41] For the as-built conditions depicted in Figures 10a, 11a, and 12, the most salient features of the streamwise force balance were the relatively large magnitudes of the pressure gradient ($4_s$) and shear stress ($5_s$) terms at the entrance to and exit from the bend. Even for the simple topography of this engineered channel, the convective acceleration terms, $1_s$ and $2_s$, on the left side of equation (4) were locally as large as the forces (pressure gradient and friction, or shear stress) on the right side. Relative to these topographically induced spatial gradients in flow velocity, cross-stream advection of momentum due to channel curvature ($3_s$) was much less significant; centrifugal accelerations made a negligible contribution to the streamwise force balance throughout the period of study.

[42] In the cross-stream direction, however, centrifugal acceleration ($3_n$) played a dominant role, causing superelevation of the water surface along the outer bank and creating a pressure gradient ($4_n$) toward the inner bank (Figure 11). Figure 12b shows that upstream of the apex, these two forces were not exactly balanced, as indicated by the gap between the lines for terms $3_n$ (red circles) and $4_n$ (black triangles). The difference between the centrifugal and

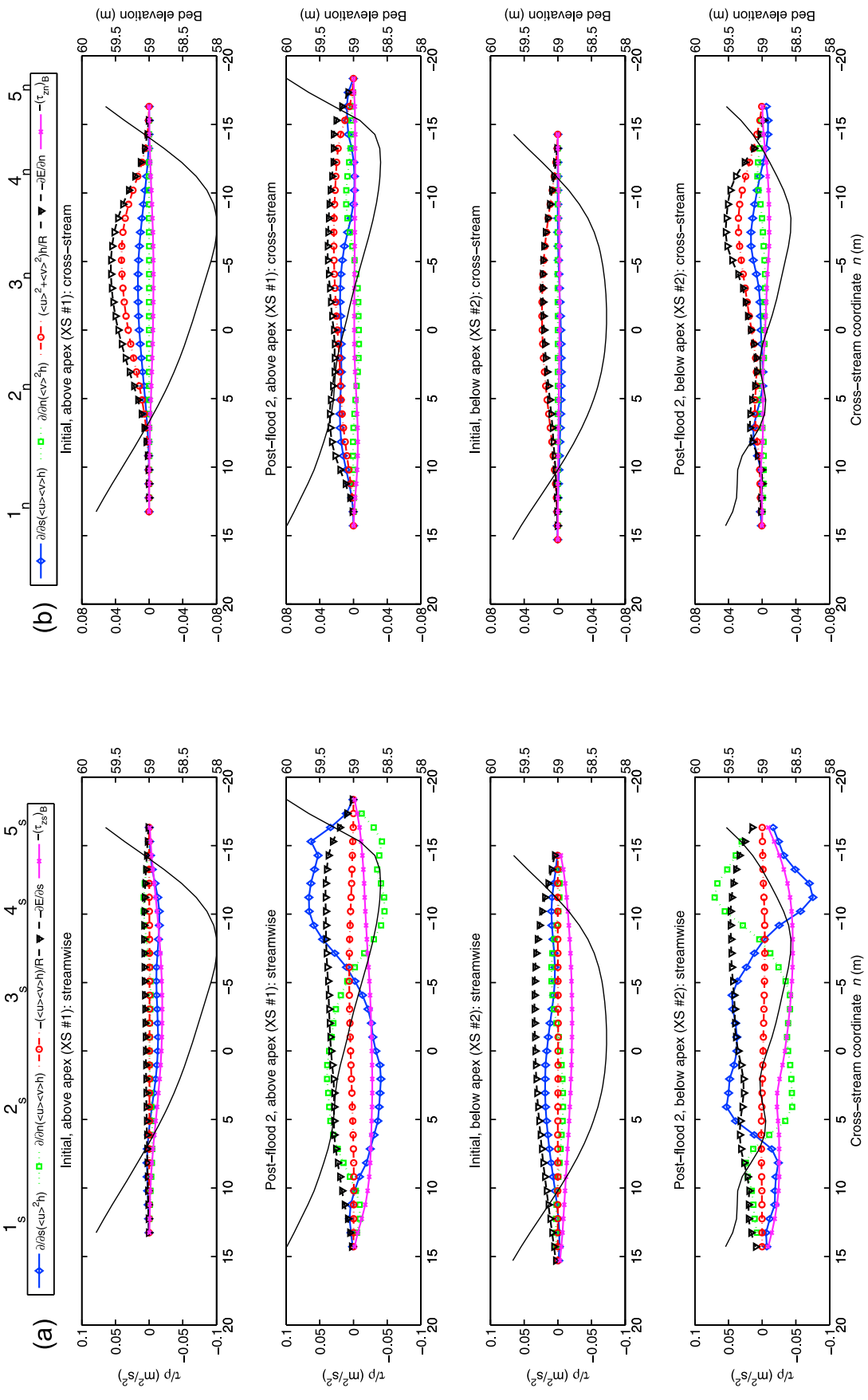


**Figure 12.** Terms in the (a) streamwise and (b) cross-stream momentum equations, plotted for cross sections upstream and downstream of the bend apex (see Figures 10 and 11 for locations) for the initial and post-flood 2 channel configurations. Bed topography is indicated by the thin black lines. Due to lack of space, the legends include only the most critical quantity in each term, but the plotted data represent values of the entire term as specified in equations (4) and (5) and listed in Table 5.

pressure gradient forces was primarily accounted for by streamwise transfer of cross-stream momentum, represented by the term labeled $1_n$ (blue diamonds). The cross-stream shear stress ($5_n$) was smaller than the other terms and stress vectors were roughly parallel to the banks.

#### 3.4.2. Pre-Flood 1

[43] Prior to the first flood event, a small bar began to form along the inner bank well upstream of the apex (Figure 9a, second column), and the adjustments to the local force balance associated with this feature are illustrated in Figures 10b and 11b. The streamwise pressure gradient ($4_s$) increased though the upstream portion of the bend, and low values of $\partial E/\partial s$ were restricted to a small region near the bend apex. The shear stress field tracked these changes in water surface slope, and the along-channel decrease in $(\tau_{zs})_B$ became less pronounced as a result of these adjustments in the pressure gradient. The new bar's most important consequence, however, was an increase in the magnitude of the convective acceleration terms ($1_s$ and $2_s$): the developing topography had begun to steer the flow.

[44] To illustrate the connection between flow patterns and the signs and magnitudes of particular components of the local force balance, consider the following, detailed interpretation of Figure 10b, first and second columns. Along the outer bank, acceleration and deepening into the apex of the bend implied a streamwise increase in streamwise momentum, reflected by positive values of $1_s$. On the other side of the channel near the inner bank, shoaling over the incipient bar caused the flow to decelerate, producing negative values of $1_s$. To understand the positive values of the term representing cross-stream transfer of streamwise momentum observed in this region, we expanded $2_s$ via the product rule to obtain

$$\frac{\partial}{\partial n}(\langle u\rangle\langle v\rangle h) = h\langle u\rangle\frac{\partial\langle v\rangle}{\partial n} + h\langle v\rangle\frac{\partial\langle u\rangle}{\partial n} + \langle u\rangle\langle v\rangle\frac{\partial h}{\partial n} \qquad (6)$$

and evaluated the sign of each term. The depth $h$ and streamwise component of the depth-averaged velocity $\langle u\rangle$ were strictly positive. For this bend to the left, outward flow corresponds to negative values of $\langle v\rangle$, which became greater in absolute value toward the outer (right) bank. Because the cross-stream coordinate $n$ also takes on more negative values toward the right bank, $\partial\langle v\rangle/\partial n$ was positive, implying that the first term on the right side of equation (6) was positive. Streamwise velocities varied less across the channel but were also greater near the right bank and smaller near the left bank, toward which $n$ took on increasingly positive values. The cross-stream derivative $\partial\langle u\rangle/\partial n$ was thus negative, and multiplying by a positive value of $h$ and a negative (outward) value of $\langle v\rangle$ yielded a positive value of the second term on the right side of equation (6). Similarly, flow was deeper toward the outside of the bend and shoaled over the incipient bar, so $\partial h/\partial n$ was negative. The product of this derivative with a positive value of $\langle u\rangle$ and a negative value of $\langle v\rangle$ was thus positive as well. All three terms on the right side of equation (6) were therefore positive, leading to positive values of the cross-stream convective term $2_s$ along the inner bank upstream of the bend apex. Applying similar reasoning to the outside of the bend, $\langle u\rangle$, $\langle v\rangle$, and $h$ were all smaller in absolute value immediately adjacent to the right bank than near the center of the channel, so $\partial\langle u\rangle/\partial n > 0$, $\partial\langle v\rangle/\partial n < 0$, and $\partial h/\partial n > 0$, resulting in negative values of all three terms in equation (6). Beginning just upstream of the apex and extending downstream, flow decelerated and began to shoal along the outer bank, resulting in negative values of $1_s$, and accelerated and deepened slightly along the inside of the bend, producing positive values of $1_s$. The cross-stream convective term $2_s$ remained opposite in sign, with streamwise momentum transferred inward along the outer bank and outward along the inside of the bend; due to conservation, a streamwise increase in momentum must be accompanied by a decrease in the $n$ direction and vice versa.

[45] The cross-stream force balance continued to be dominated by the centrifugal term ($3_n$) and pressure gradient ($4_n$). The lateral tilt of the water surface was greater than during the first time period, resulting in a larger pressure gradient force that was not entirely balanced by the centrifugal acceleration, as indicated by a comparison of Figure 11b, third and fourth columns. The difference between these two terms was primarily satisfied by a larger, positive value of $1_n$, indicating an along-channel increase in cross-stream momentum due to outward steering of the flow by the incipient bar. The shear stress term ($5_n$) was much smaller than the centrifugal ($3_n$), pressure gradient ($4_n$), and streamwise convective terms ($1_n$), with weak outward directed stresses on both the upstream and downstream limbs of the bend. The cross-stream stress was larger and inward through the middle of the bend, with the greatest values of $(\tau_{zn})_B$ on the right (outer) side of the channel just upstream of the apex.

#### 3.4.3. Between Floods

[46] The point bar that had begun to form along the inner bank grew significantly during the 2005 flood (Figure 5) and began to present a more substantial obstacle to the flow. Figure 10 shows that the development of the morphology accentuated the modifications to the local force balance initiated prior to this event. A rise in the water surface elevation upstream of the bar reduced the streamwise pressure gradient over the upstream portion of the bend and increased $\partial E/\partial s$ through the apex and downstream portion of the meander. The higher water surface elevation along the inner bank also reduced the transverse pressure gradient. This effect of the growing bar was illustrated by comparing the maps in Figures 12b and 12c, fourth column: following the first flood event, $\partial E/\partial n$ decreased over the head of the bar and increased near the apex, where superelevation along the outer bank was greatest. The darker red tones in Figure 11c, fourth column, than in Figure 11c, third column, also indicate that these lower values of $\partial E/\partial n$ in the upstream portion of the bend were exceeded by the centrifugal force.

[47] Topographically induced convective accelerations contributed to changes in the flow field as well. Figure 10c indicates that bar growth resulted in more coherent, broader zones with larger values of these terms: $1_s$ and $2_s$ were of greater magnitude than the pressure gradient force for most of the bend. The shoaling and deceleration that occurred as the flow approached the bar produced negative values of the streamwise convective term $1_s$ along the inner bank upstream of the apex. Past the apex, positive values of $1_s$ occurred near the inner bank where the flow became deeper on the downstream side of the bar. Conversely, on the right side of the centerline toward the outer bank, $1_s$ was positive upstream of the apex as the flow deepened into the pool and

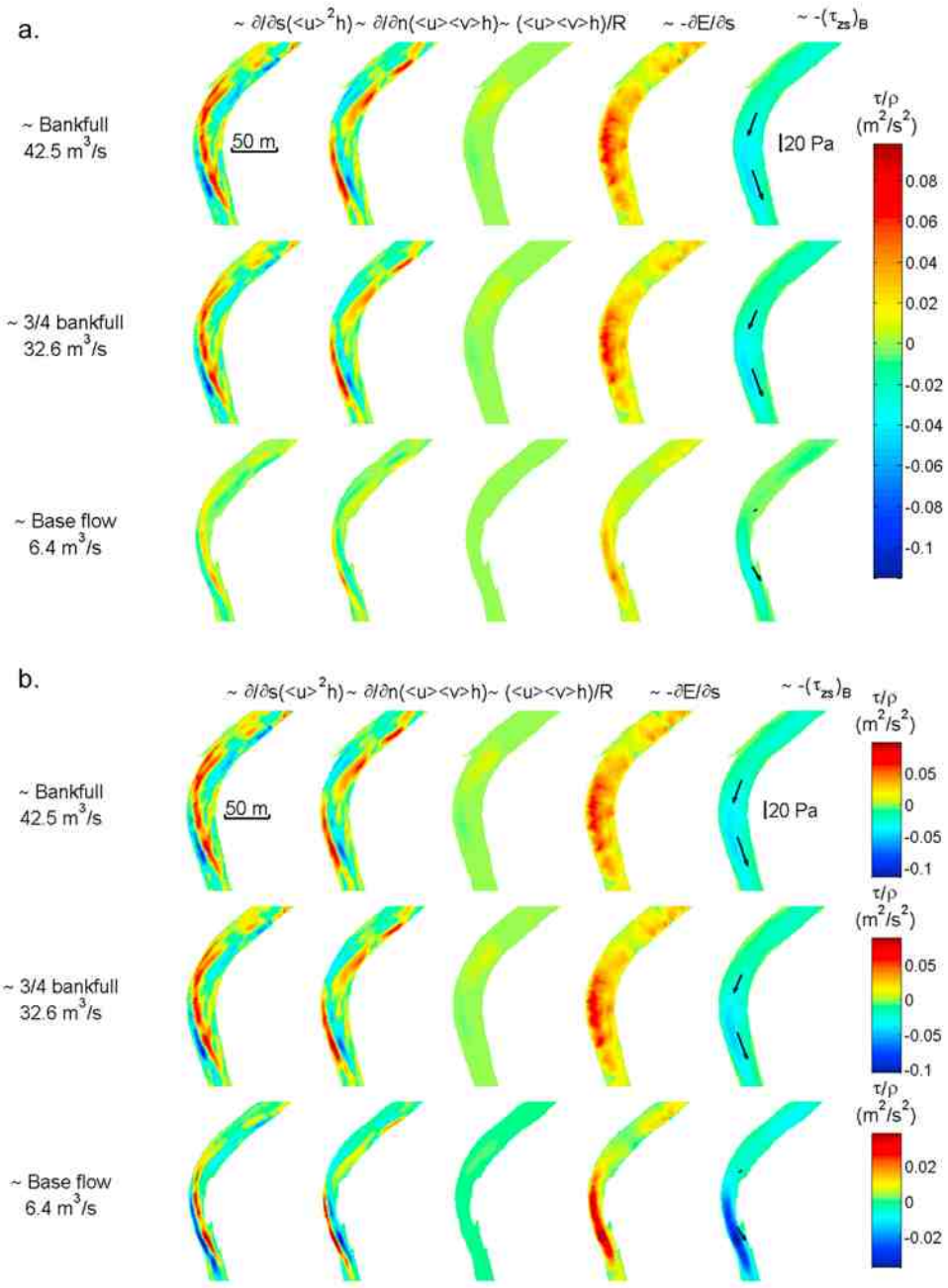


**Figure 13.** Stage dependence of streamwise force balance components. (a) (top) Approximately bankfull, (middle) approximately 3/4 bankfull, and (bottom) approximately base flow. Each column represents a term in the momentum equation. A common color scale is used for all three discharges. (b) Same as Figure 13a but a separate color scale is used for each discharge. Due to lack of space, the heading for each column includes only the most critical quantity in each term, but the plotted data represent values of the entire term as specified in equation (4). The boundary shear stress vectors along the channel centerline upstream and downstream of the bend apex are indicated in the fifth column.

negative past the apex where the bed began to rise toward the riffle downstream. Throughout the bend, the cross-stream convective term $2_s$ remained similar in magnitude but opposite in sign from $1_s$. Similarly, for the cross-stream force balance, Figure 11c indicated that the reduced transverse pressure gradient was associated with an increased streamwise transfer of cross-stream momentum (i.e., larger values of $1_n$).

#### 3.4.4. Post-Flood 2

[48] Overall, the channel changes that occurred during the second flood were relatively minor (Figure 5), and a comparison of Figures 10c and 10d and 11c and 11d indicates that the components of the local force balance were not modified substantially by the 2006 event. The most notable differences involved the convective acceleration terms $1_s$ and $2_s$ in equation (4). A strengthening of the high-velocity

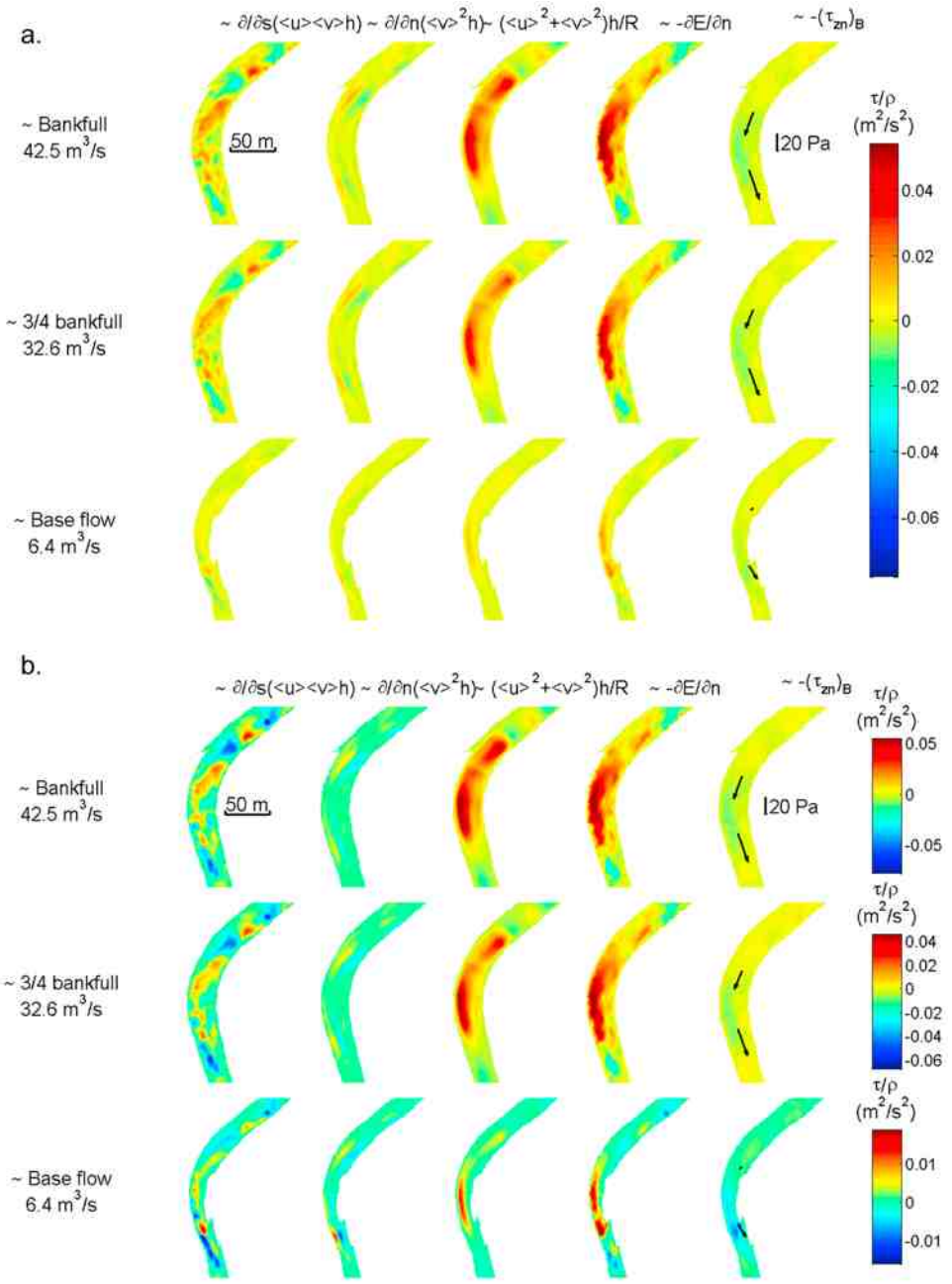


**Figure 14.** Stage dependence of cross-stream force balance components. (a) Same as Figure 13a. Each column represents a term in the momentum equation. A common color scale is used for all three discharges. (b) Same as Figure 14a but a separate color scale is used for each discharge. Due to lack of space, the heading for each column includes only the most critical quantity in each term, but the plotted data represent values of the entire term as specified in equation (5). The boundary shear stress vectors along the channel centerline upstream and downstream of the bend apex are indicated in the fifth column.

core, particularly near the outer bank downstream of the bend apex (Figure 9), intensified along-channel transfer of streamwise momentum. This adjustment of the flow field was reflected by a more pronounced zone of large positive values of $1_s$ that formed a narrow but continuous swath shifting laterally across the channel from the outer bank upstream of the apex (Figure 12b, second row) toward the inner bank downstream of the apex (Figure 12d, fourth row). The magnitude of the cross-stream convective term $2_s$ in the streamwise force balance also increased downstream of the bar, but overall the spatial pattern of the terms in equation (4) was very similar before and after the 2006 flood. One notable difference that highlighted the importance of convective accelerations was the reduction in the streamwise pressure gradient to very low or negative values upstream of the bar near the entrance to the bend. The small to adverse water surface slope in this area implied that down stream flow through this region was instead driven by

the inertial forces associated with the fluid's momentum [*Dietrich and Smith*, 1983]. Figures 11c and 11d indicate that the cross-stream force balance also changed little following the second flood event.

### 3.5. Effects of Flow Stage on the Local Force Balance

[49] Prior analyses of the significance of topographic steering effects have been conducted at flow stages significantly below bankfull; *Dietrich and Smith* [1983] reported measurements from 70% of bankfull and *Whiting* [1997] compared data collected at 30 and 45% of the bankfull stage. To assess the extent to which the components of the local force balance varied as a function of flow stage, we analyzed FaSTMECH runs corresponding to the bankfull discharge, 75% of bankfull, and base flow conditions. These model runs were based on topographic data collected following the second flood event, by which time the bar-pool morphology was well established. In Figures 13 and 14, each row represents one of the modeled discharges and each column corresponds to a term in the streamwise or cross-stream momentum equation. To assess the relative magnitudes of the various forces across this range of flows, we created force balance maps with a color scale common to all three discharges; these maps are shown in Figures 13a and 14a. In Figures 13b and 14b, a separate color scale was used to create force balance maps for each flow we considered; this representation allowed us to more effectively visualize and interpret the relative significance of force balance components for a given discharge.

[50] At lower stages, one might expect that channel morphology would exert a stronger influence on the flow and that topographically induced spatial gradients of velocity would thus play a more prominent role in the local force balance. At higher stages, greater flow depths might tend to drown out the topography and reduce the importance of these convective terms relative to other forces. The one previous study to explicitly examine the effects of stage on the force balance of which we are aware [*Whiting*, 1997] generally supported these hypotheses: convective accelerations were found to be less important at a higher flow stage. The two discharges considered by *Whiting* [1997] were well below bankfull, however, and his study was conducted on a short, straight reach of a smaller stream with a midchannel bar rather than a point bar.

[51] In contrast with *Whiting*'s [1997] observations, our results showed that in a larger, gravel bed meander bend with a well-developed point bar, convective accelerations remained important for discharges up to and including the bankfull flow. The use of a common color scale in Figures 13a and 14b illustrated that force magnitudes were larger at higher discharges than under base flow conditions. For the lowest modeled stage, the area in which the magnitudes of the convective acceleration and pressure gradient terms in the streamwise force balance were comparable to those observed at the higher discharges was restricted to a small zone downstream of the bend apex. In the cross-stream direction, the centrifugal acceleration and pressure gradient terms were considerably smaller for the lowest stage because flow depths and velocities were lower. For both the streamwise and cross-stream balances, force maps for the 3/4 bankfull and bankfull flows exhibited consistent patterns, even with the common color scale. This result implied that the flow field and force balance at a lower stage would be very similar to the bankfull conditions described above.

[52] Greater insight regarding the stage dependence of the force balance was gained by inspecting Figures 13b and 14b, in which a separate color scale was used for each modeled discharge. The zone of low values of the streamwise pressure gradient at the upstream end of the bar was more extensive at the lowest stage, when the bar more effectively obstructed the flow and caused a more pronounced rise in water surface elevation upstream of the bar. This hydraulic response not only increased pressure over the bar but also reduced the degree of superelevation along the outer bank; both of these effects contributed to lower values of the cross-stream pressure gradient in this region. For the cross-stream force balance, relatively (for a given discharge) large values of the centrifugal and pressure-gradient terms were thus restricted to the immediate vicinity of the bend apex under base flow conditions but extended farther upstream and downstream for stages closer to bankfull, when velocities were higher and the bar presented a less significant obstacle to the flow.

[53] Spatial velocity gradients induced by the morphology were clearly significant at all three stages, but were smaller under base flow conditions. For the lowest discharge, relatively (for that flow) large values of the convective terms in the streamwise force balance occurred over a smaller portion of the bend than at higher stages. The strong convective accelerations observed at the upstream end of the point bar for flows approaching bankfull were much less evident at the lower stage, implying that not only velocities but also velocity gradients, and therefore accelerations, were greater at higher flows. This finding contrasts with a previous study of a midchannel bar, where velocities were greater at a higher stage but accelerations were more gradual [*Whiting*, 1997]. We also observed that for the cross-stream balance, streamwise transfer of cross-stream momentum was an important effect for all three discharges. In general, the key result to emerge from our investigation of the stage dependence of the force balance was that topographically induced convective accelerations played a prominent role at discharges up to and including the bankfull flow: the bar-pool morphology exerted a strong influence on the flow field even when that morphology was fully submerged by the flow.

## 4. Discussion

### 4.1. Connecting the Local Force Balance to the Evolution and Stability of Channel Form

[54] Section 3.4 examined individual force balance components and their interactions at four time points during the morphologic evolution of the Robinson Reach. Here, we synthesize these observations and use them to address a basic geomorphic question: what do the observed changes in the local force balance imply for the adjustment of channel form? In keeping with our focus on the effects of point bar development, the following discussion is organized into three phases: (1) bar formation, corresponding to the simple, initial channel configuration described in section 3.4.1; (2) bar building, represented by the pre-flood 1 and between flood intervals (sections 3.4.2 and 3.4.3); and (3) bar maintenance, associated with the post-flood 2 time period

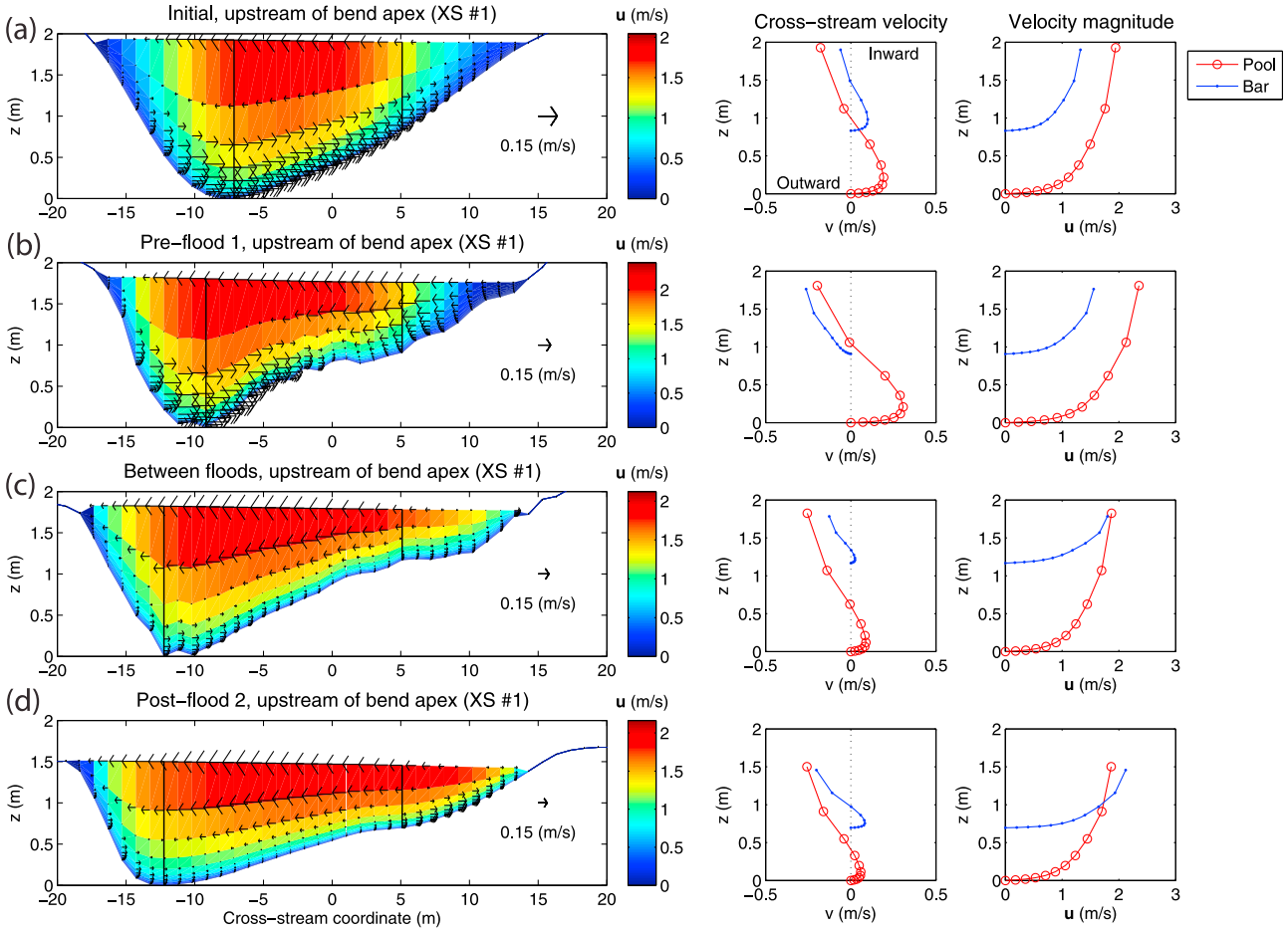


**Figure 15.** (left) Quasi-3-D flow solutions from FaSTMECH numerical model runs for a bankfull discharge of 42.5 $m^3/s$ from a cross section upstream of the bend apex (see Figures 10 and 11 for location). Different time period during the morphologic evolution of the Robinson Reach: (a) Initial, (b) pre-flood 1, (c) between floods, and (d) post-flood 2. (middle and right) The solid vertical lines in each cross section indicate the pool and bar locations from which the vertical profiles of flow velocity were extracted. The pool profile was obtained from the deepest point along the cross section for each time period, but the bar profile was taken from the same location for all time periods. The vertical coordinate is referenced to the deepest point along the cross section for each time period, not to an absolute, consistent datum.

(section 3.4.4). To illustrate the adjustments in the flow field that occurred during this progression, we extracted a pair of cross sections from the numerical model's quasi-3-D flow solution for a bankfull discharge. The transects shown in Figures 15 and 16 were taken upstream and downstream of the apex of bend 1, respectively (see Figures 10 and 11 for locations). By depicting the manner in which the magnitude and transverse component of the velocity vector **u** varied across the channel and vertically over the flow depth, these plots highlighted the influence of bar development on secondary circulation within the bend. Topographic steering effects played a prominent role throughout the measured sequence of channel configurations, consistent with force balance analyses indicating that convective accelerations were among the dominant terms in equations (4) and (5). In essence, enlargement of the bar directed greater amounts of fluid momentum toward the concave bank, modifying patterns of flow and sediment transport to establish, modify, and ultimately maintain the bar form. In general, results from our study of a relatively large, gravel bed river were in accordance with previous investigations of the influence of point bars on velocity and shear stress fields in smaller, sand-bedded meander bends [e.g., *Dietrich and Smith*, 1983].

### 4.1.1. Bar Formation

[55] This reengineered segment of the Merced River provided an opportunity to examine, at field scale, a simple channel with a known initial condition that featured a sinuous planform but had gentle, planar cross-stream bed slopes rather than well-developed bar forms. For the as-built configuration of the Robinson Reach, the balance of forces described in section 3.4.1 established a flow field conducive to the deposition of bed material along the inside of meander bends. Flow conditions along this reconstructed channel were well approximated by simple models of bend flow in which the centrifugal force ($3_n$) causes superelevation along the outer bank, establishing a cross-stream pressure gradient ($4_n$) toward the inner bank. The interaction of these two forces drives helical flow in which velocity vectors are directed inward near the bed and outward near the water

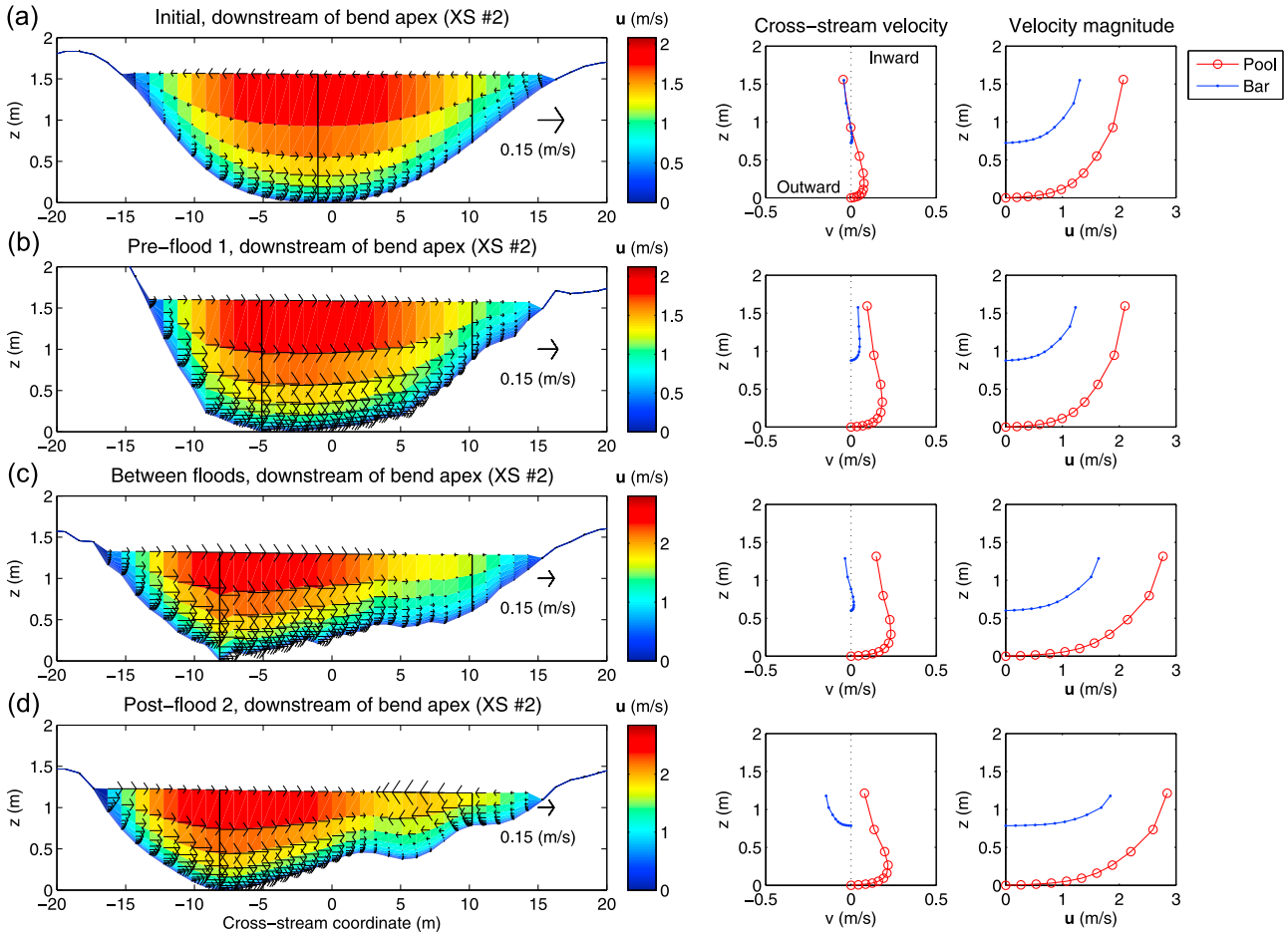


**Figure 16.** (left) Same as Figure 15 except quasi-3-D flow solutions from FaSTMECH numerical model runs for a bankfull discharge of 42.5 $m^3/s$ from a cross section downstream of the bend apex (see Figures 10 and 11 for location). (middle and right) The solid vertical lines in each cross section indicate the pool and bar locations from which the vertical profiles of flow velocity were extracted. The pool profile was obtained from the deepest point along the cross section for each time period, but the bar profile was taken from the same location for all time periods. The vertical coordinate is referenced to the deepest point along the cross section for each time period, not to an absolute, consistent datum.

surface; this secondary circulation pattern is illustrated by a cross section from upstream of the bend apex, shown in Figure 15a. At this early stage of morphologic evolution, near-bed velocities were inward across the full width of the channel through the apex of the bend. Output from the numerical flow model indicated positive values of the cross-stream component of boundary shear stress $(\tau_{zn})_B$, implying sediment transport toward the left (inner) bank. These results were consistent with theoretical models in which deposition is concentrated on the convex bank due to inward near-bed flow driven by the helical circulation [e.g., *Dietrich*, 1987]. Because the magnitude of the centrifugal force varies inversely with the radius of curvature, this secondary flow is strongest at the bend apex, where $R$ reaches a minimum, and the greatest deposition would be expected to occur in this location.

[56] Sediment transport in the streamwise direction also plays a role, however. Even for the special case of a perfectly flat bed examined by *Nelson and Smith* [1989a], streamwise divergence of the sediment flux results from changes in the streamwise pressure gradient, and hence $(\tau_{zs})_B$, due to along-channel variation in $R$. Along the inner bank, a given elevation drop occurs over a shorter distance in a more strongly curved reach where $R$ is smaller, resulting in a higher slope and contributing to a greater stress. Conversely, for a bend of lower curvature (larger $R$), the same elevation loss would occur over a longer distance, so the slope and shear stress would be reduced. Approaching the apex from upstream, the decrease in $R$ thus causes $\partial E/\partial s$ to increase downstream along the inner bank, leading to erosion. Downstream of the apex, $R$ increases and creates a downstream-decreasing pressure gradient and hence deposition. When superimposed upon the dominant cross-stream, inward convergence of sediment, these streamwise effects tend to reduce deposition upstream of the apex and augment deposition downstream of the apex; the point bar is thus predicted to grow most rapidly just downstream of the apex [*Nelson and Smith*, 1989a]. On the Robinson Reach, this idealized pattern was complicated by the abrupt, engineered decrease in the water surface slope near the entrance to the bend, which dictated a downstream decrease in boundary shear stress and caused deposition (Figure 9). The water

surface slope increased again just downstream of the apex and produced a slight downstream increase in stress, which would tend to produce erosion. As a result, point bar formation was expected to occur not immediately downstream of the apex, as predicted for a perfectly flat bed, but rather upstream of the apex where $\partial(\tau_{zs})_B/\partial s$ was negative. In addition, the FaSTMECH results shown in Figure 16a indicated very weak cross-stream flow downstream of the apex that would not have been sufficiently powerful to transport sediment toward the inner bank (the Shields stress computed from the maximum value of $(\tau_{zn})_B$ along this cross section was 0.0046, well below the threshold for entrainment), thus limiting the streamwise extent of the bar. The measured topography for the next increment in our time series was consistent with this hypothesized pattern of deposition: a small, incipient bar formed along the inner bank well upstream of the apex.

#### 4.1.2. Bar Building

[57] The bed topography defined by this nascent deposit exerted a strong influence on the local force balance and, in so doing, fostered continued bar growth even before the Robinson Reach had experienced any significant flood events. The pre-flood 1 time period thus represented an early stage of point bar development, and the dominant terms in the streamwise force balance during this phase were the convective accelerations and pressure gradient, with friction along the channel boundary (i.e., shear stress) playing a smaller role. In the cross-stream direction, the centrifugal and pressure gradient terms remained greatest in magnitude but were not exactly balanced, with the difference primarily accommodated by increased streamwise transfer of cross-stream momentum ($1_n$). The incipient bar, with a topographic relief index of 1.53, thus had a significant effect on the flow field, producing a shear stress pattern that favored additional deposition of bed material to build the bar longitudinally. The streamwise reduction in $\partial E/\partial s$ approaching the apex of the bend shown in Figure 10 implied a downstream decrease in $(\tau_{zs})_B$ and hence deposition in the central portion of the bend. Because this decrease in stress occurred further downstream during this time period than for the initial survey, sediment accumulation was expected to be focused closer to the apex. The model results shown in Figures 15b and 16b indicated that near-bed flow in the thalweg and along the outer bank was directed inward due to strong secondary circulation within the pool. The vertical profiles of cross-stream velocity in Figure 15b, second column, clearly illustrate this pattern of secondary flow: outward over the bar and close to the water surface in the thalweg, coupled with high near-bed velocities toward the inner bank in the pool and on the lower portion of the bar. The cross-stream shear stress in this region was thus relatively large and oriented toward the inside of the bend, implying that deposition would remain concentrated along the inner bank at and downstream of the bend apex, allowing the bar to extend farther along the channel.

[58] Upstream of the apex, the developing topography dictated a flow pattern that inhibited further increases in bar height but enabled the bar to grow laterally while also providing a mechanism for diverting sediment around the bar and into the adjacent pool. This flow pattern is clearly illustrated in Figure 15b: velocities over the upstream shoulder of the incipient bar were directed outward not only near the water surface but throughout the full flow depth. This hydraulic adjustment reflects a weakening of the secondary circulation that can be explained as follows. Upon encountering the bar, flow along the inner bank shoaled and decelerated, resulting in an increase in pressure over the head of the bar, described by *Nelson and Smith* [1989a] as the Bernoulli response of the flow to the bar. A corresponding increase in the streamwise transfer of cross-stream momentum, reflected by larger values of $1_n$ (Figure 11b, first column), also contributed to a rise in water surface elevation over the bar and drop over the pool [*Dietrich and Smith*, 1983]. As a result, the cross-stream tilt of the water surface through the upstream portion of the bend was reduced relative to the $\partial E/\partial n$ values observed during the earlier stages of bar development, as indicated by Figure 11, fourth column, and Figures 12b, first and second rows. The diminished transverse pressure gradient was exceeded by the centrifugal acceleration, which acted to drive the flow outward, away from the bar. Similarly, although the streamwise convective terms $1_s$ and $2_s$ were similar in magnitude but opposite in sign and thus tended to cancel one another, such that the magnitude of the local boundary shear stress was approximately equal to that of the local pressure gradient, these topographically induced convective accelerations played an important role in reorienting the boundary shear stress vector toward the outer bank. The net effect was a weakening of the secondary circulation, with velocities directed outward even near the bed. Figure 16b indicates that this flow pattern had not been established downstream of the bend apex, however. Downstream of the incipient bar, velocities were weak but inward throughout the water column. In the upstream portion of the bend, the point bar produced an outward transfer of momentum that caused the high-velocity core and maximum shear stress to shift across the centerline farther upstream and more abruptly than when the bed was more nearly flat.

[59] The channel changes documented via the next data set in our topographic time series, a survey conducted following the 2005 flood, illustrated the morphologic response to these hydraulic adjustments. Considerable bar growth occurred during this period of prolonged high flows, and the topographic relief index increased to 1.79; *Dietrich and Smith* [1983] reported a similar value of 1.8 for their sand-bedded Muddy Creek site. At this stage in the evolution of the Robinson Reach, the morphology was effectively routing the flow around the upstream end of the bar and obliquely across the channel: this is the essence of topographic steering. By the end of the 2005 flood event, the bar had grown to such a degree that these topographic effects limited further deposition on the bar top and instead acted to convey bed material around the bar and into the pool. Some of this sediment accumulated along the inside of the bend at and downstream of the apex, leading to an increase in both the lateral and longitudinal extent of the bar (Figure 5). This enlargement of the bar modified the flow field downstream of the apex as shown in Figure 16c, which indicates that cross-stream velocities had weakened near the bed and were outward closer to the water surface. Upstream of the apex, vertical growth of the bar caused shoaling of the flow and an increase in the velocity gradient (Figure 15c, third column), leading to greater shear stress and hence erosion of, rather than deposition on, the bar top. In addition, Figure 15

indicates that outward directed flow continued to prevail over the upstream end of the bar, implying that both gravitational and fluid drag forces would direct sediment away from the bar. As discussed by *Nelson and Smith* [1989a] and *Dietrich and Whiting* [1989], the resulting particle trajectories included a cross-stream component toward the pool neglected by models that consider only a balance between the particle weight, directed outward down the bar slope, and the inward fluid drag associated with curvature-induced secondary circulation [e.g., *Ikeda*, 1989]. Further increases in bar height were thus expected to be minor, with any additional deposition focused not on top of the bar but rather along its margin or in the adjacent pool.

#### 4.1.3. Bar Maintenance

[60] Topographic adjustments associated with the second, 2006 flood event were, in fact, relatively minor, with only a slight change in the topographic relief index from 1.79 to 1.75. Figure 5 indicates that small amounts of deposition occurred on the upstream flank and outer margin of the point bar, consistent with the hypothesized topographic steering of bed material away from the bar top. More sediment was instead deflected laterally toward the thalweg, and an increase in boundary shear stress along the outer bank downstream of the bend apex (Figure 12d, left) allowed this material to be conveyed through the pool. Morphologic response to the latter flood was thus less pronounced, despite its greater peak discharge and duration of overbank flow (Figure 2), and the modest changes that did occur had little impact on the local force balance. These observations implied that by the end of the 2005 event, the channel had attained a stable configuration more nearly in equilibrium with the prevailing conditions of flow and sediment supply. Sediment budget calculations reported elsewhere (L. R. Harrison et al., Channel dynamics and habitat development in a meandering, gravel bed river, submitted to *Water Resources Research*, 2009) indicate that the amount of bed material supplied to the Robinson Reach during the 2006 flood was only 58% of that supplied in 2005. These results suggest that in addition to the internal dynamics emphasized herein, a key external driver (sediment supply) also played a role in stabilizing the bar form. In any case, at this stage in the river's evolution, the bar had progressed through phases of formation and growth and was approaching a state of self-maintenance. For example, the vertical profile in Figure 15d, third column, indicates high-velocity magnitudes and steep velocity gradients over the upstream shoulder of the bar that would act to prevent further deposition in this region. In addition, the numerical flow model results depicted in Figure 15 show that secondary circulation had reestablished upstream of the bend apex, with velocities over the upstream end of the bar once again directed inward near the bed. FaSTMECH output also provided evidence that topographic steering effects had become significant throughout the bend: Figure 16d shows a cross section downstream of the apex in which cross-stream velocities over the bar were directed outward over the entire depth of flow, implying shear stress and sediment transport vectors oriented away from the tail of the bar and toward the channel thalweg. The occurrence of this pattern at the downstream end of the existing bar would also allow for lateral and downstream migration of the bar form, particularly when coupled with the observed erosion of the outer bank (Figure 5).

[61] These results can be integrated into a conceptual model for the maintenance of a stable bar-pool morphology. Initially, point bar growth occurred because sediment was delivered to the bar more rapidly than it was removed. As the bar developed, primarily as a result of the first flood, the rising bed topography reduced the cross-stream pressure gradient and allowed the centrifugal force to direct the flow outward, routing sediment away from the bar top and into the pool. The topographically induced convective accelerations associated with this steering effect thus provided a mechanism by which an equilibrium channel configuration could be established [*Dietrich and Whiting*, 1989]. If streamwise transport of sediment along the inner bank and up onto the bar were to increase without a corresponding increase in cross-stream transport into the pool, deposition on top of the bar would increase its amplitude; that is, the bed elevation difference between bar and pool would become greater. This morphologic adjustment would intensify the topographic steering effect and thus accelerate cross-stream transport into the pool. Conversely, if increased lateral transport into the pool were not matched by more rapid delivery of bed material to the bar top, the elevation difference between bar and pool would be reduced. The influence of the topography on the flow would be lessened as a result, which would allow the helical circulation to strengthen, producing inward near-bed velocities that would convey sediment toward the inner bank and lead to an increase in bar height. In their study of a small, sand-bedded meander, *Dietrich and Smith* [1983] concluded that an equilibrium point bar amplitude was achieved when the streamwise decrease in sediment transport along the inner bank onto the bar was balanced by an increase in topographically induced outward transport of bed material into the pool. Our measurements and calculations from a larger, gravel bed river supported this hypothesis and demonstrated that convective accelerations played a prominent role in developing and maintaining a stable bar-pool morphology in this environment as well.

### 4.2. Coupling Hydraulic and Morphologic Adjustments at the Reach Scale

[62] In this section, we take a step back from detailed analyses of the local force balance and interpret the channel changes observed along the Robinson Reach in terms of the coupling between the flow field and the evolving morphology. To summarize the manner in which these form-process interactions were manifested at a larger, reach scale, we examined the relationship between sediment deposition and the magnitude and spatial pattern of the boundary shear stress. For each successive pair of topographic data sets, a streamwise series of deposition volume per unit channel length was obtained by integrating positive bed elevation differences (Figure 5) across the channel, taking care to account for the variation in cell size with transverse position due to curvature. FaSTMECH model output for each time period was used to determine the maximum boundary shear stress $\tau_{max}(s)$ for each cross section along the channel and the transverse position $n_{max}$ at which this maximum occurred. Previous studies of flow patterns through meander bends have emphasized the development of a focused band of high velocities and boundary shear stresses that shifts from the inside to the outside of the channel over the course

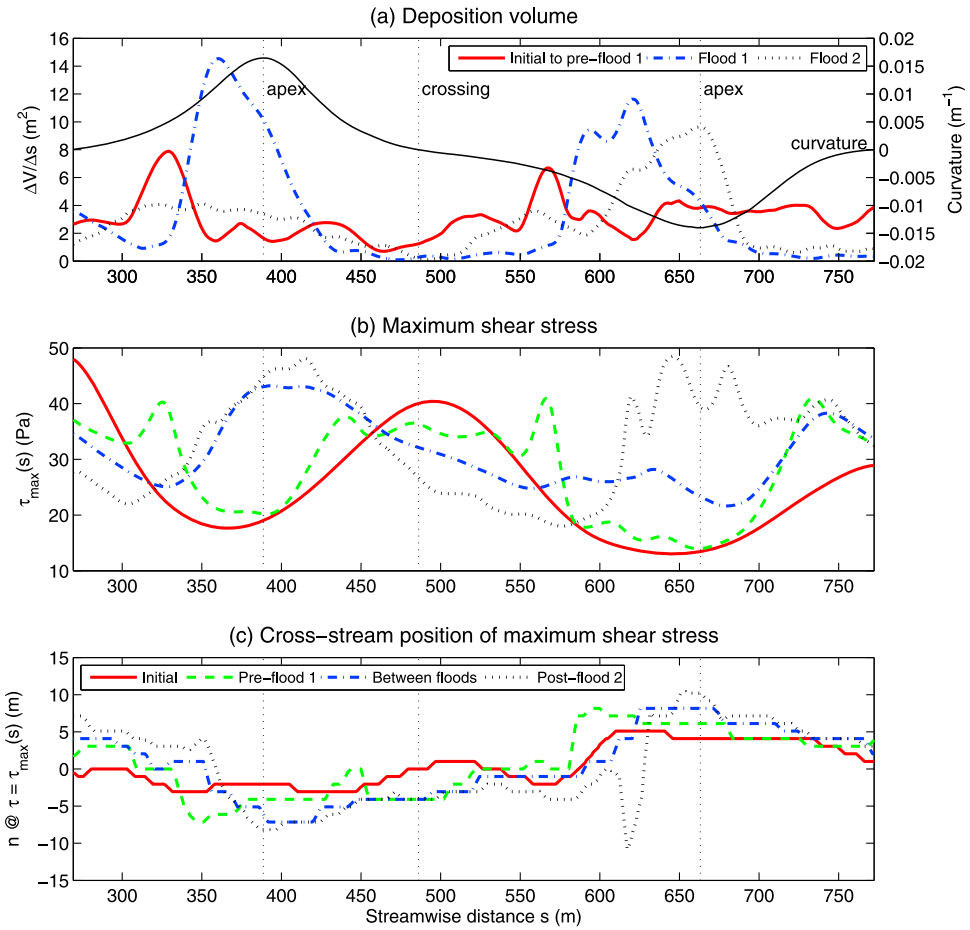


**Figure 17.** Streamwise series of (a) deposition volume per unit channel length provided an index of bar growth while series of (b) maximum boundary shear stress and (c) the cross-stream position at which this maximum occurred summarized the effects of bar development on the flow field. The legend in Figure 17c applies to Figure 17b as well.

of the bend. One of the principal effects of the point bar noted by these workers is to strengthen this high-velocity core and cause the zone of maximum boundary shear stress to shift laterally toward the outer bank more abruptly and further upstream than would occur if the bar were absent [e.g., *Dietrich and Smith*, 1983; *Nelson and Smith*, 1989a; *Dietrich and Whiting*, 1989]. Our data provided a test of this hypothesis in a larger, gravel bed river.

[63] Point bar development along the Robinson Reach is illustrated in Figure 17a, which shows the formation of incipient bars at the upstream end of each bend prior to the first flood event, the large sediment volumes deposited on these bars during the 2005 flood, and the relatively minor growth of the first bar and much greater development and downstream translation of the second bar during the 2006 flood. Figure 17b indicates that these patterns of bar growth exerted a strong influence on the magnitude and spatial pattern of the boundary shear stress. For the initial channel configuration lacking bars, the largest values of $\tau_{max}(s)$ were located in riffles, but even the minor bar development that occurred prior to the first flood caused the peaks in $\tau_{max}(s)$ to translate downstream toward the entrance to each bend, where bed material had begun to accumulate. Figure 17c indicates that the cross-stream position of maximum shear stress, which had been near the channel centerline for the constructed topography, shifted toward the outer bank just downstream of the spikes in deposition volume. During the first flood, large amounts of bed material were deposited downstream of the nascent bars that had formed prior to the event. For the first bend, $\tau_{max}(s)$ increased considerably and peaked just past the bend apex, downstream of the maximum deposition volume. The cross-stream position of $\tau_{max}(s)$ remained near the centerline for a greater distance along the channel than before the first flood, shifted to a similar $n$ coordinate past the apex, and stayed closer to the outer bank farther into the downstream portion of the first bend before crossing the centerline again. For the second bend, a smaller volume of sediment was deposited further upstream (relative to the bend apex) and $\tau_{max}(s)$ did not increase through the second bend as it did for the first. During the second flood, additional deposition on the first bar was minor but a much greater volume of bed material accumulated on the second bar, at a position farther downstream than during the first event. In the first bend, $\tau_{max}(s)$ changed little after the second flood but $n_{max}(s)$ was closer to the left (inner) bank over the upstream end of the bar and then shifted more abruptly toward the right (outer) bank. In the second bend, bar growth during the 2006 flood caused a

pronounced increase in $\tau_{max}(s)$ and $n_{max}(s)$ occurred closer to the outer bank at a position further upstream than after the 2005 flood. The prominent negative spike in the post-flood 2 series of $n_{max}$ values upstream of the apex of the second bend was due to the development of a zone of high shear stress near the inner bank along the upstream shoulder of the bar.

[64] In summary, these results indicated a positive correlation between the volume of sediment deposited on point bars and the magnitude of the boundary shear stress through the bend. Moreover, greater deposition volumes were associated with a more abrupt shift of the cross-stream position of maximum shear stress to a location nearer the outer bank. Our observations from a larger gravel bed river were thus consistent with prior studies of flow patterns in smaller, primarily sand-bedded channels. In both environments, a strong coupling existed between channel morphology and hydraulics; this is the essence of an alluvial river.

## 5. Conclusion

[65] This study examined interactions between the flow field and an evolving channel morphology for a gravel bed river at flows up to bankfull. To gain insight regarding the mutual adjustment of topography and hydraulics that takes place as a stable channel geometry develops and is ultimately maintained, we focused our attention on the balance of forces governing the flow field. A quasi-three-dimensional numerical flow model was used to evaluate individual terms in the streamwise and cross-stream momentum equations and quantitatively map the components of the local force balance. This approach allowed us to examine the significance of topographically induced convective accelerations at different stages of bar development and as a function of flow stage. Our results thus provided insight on the interactions between the flow field and the morphology that occurred as a simple, meandering river gradually developed more complex topography. The principal conclusions arising from this investigation include the following:

[66] 1. The development of point bars in this simple, meandering river was gradual, coherent, and well organized, as were their effects on the flow field. Our observations from a larger, gravel bed river were thus consistent with geomorphic theory developed primarily through flume experiments, numerical models, and field studies in smaller, sand-bedded channels.

[67] 2. Even for the initial, engineered channel, which had planar cross-stream bed slopes and lacked bars, force balance analyses based on output from a numerical flow model indicated that convective accelerations driven by the topography were of a similar magnitude to the streamwise pressure gradient force and boundary shear stress.

[68] 3. The convective terms in the streamwise and cross-stream momentum equations took on a more prominent role in the local force balance as point bars grew over time. Bar development was the primary factor leading to the establishment of topographic steering effects that in turn acted to maintain the form of the channel.

[69] 4. As the bars formed and became larger, the developing topography modified the balance of forces so as to route flow and sediment around the upstream end of the bar and obliquely across the channel. The river evolved toward a stable bar-pool morphology as streamwise transport along the inner bank and up onto the bar was balanced by topographically induced cross-stream transport off the bar and into the pool.

[70] 5. Convective accelerations associated with the bed topography remained significant at stages up to and including bankfull, a result that was not apparent in earlier field studies conducted at lower discharges.

[71] **Acknowledgments.** This investigation was funded by a grant from the CalFed Bay Delta Authority Science Program and was performed in collaboration with the California Department of Water Resources (CDWR). Kevin Faulkenberry and David Encinas of the CDWR provided logistical support and design information for the Robinson Reach, and the CDWR staff assisted in the field work. Aleksandra Wydzga and José Constantine helped with field surveys. Jon Nelson and Rich McDonald, who developed the MD-SWMS/FaSTMECH flow model, provided valuable implementation advice. Steve Darby, Peter Whiting, Filip Shurman, Martin Kleinhans, Rob Ferguson, Michael Church, and two anonymous reviewers provided useful comments on earlier versions of this paper.

## References

Barton, G. J., R. R. McDonald, J. M. Nelson, and R. L. Dinehart (2005), Simulation of flow and sediment mobility using a multidimensional flow model for the white sturgeon critical-habitat reach, Kootenai River near Bonners Ferry, Idaho, *U.S. Geol. Surv. Sci. Invest. Rep.*, *2005–5230*, 54 pp.

Blanckaert, K. (2010), Topographic steering, flow recirculation, velocity redistribution, and bed topography in sharp meander bends, *Water Resour. Res.*, *46*, W09506, doi:10.1029/2009WR008303.

Blanckaert, K., and H. J. de Vriend (2003), Nonlinear modeling of mean flow redistribution in curved open channels, *Water Resour. Res.*, *39*(12), 1375, doi:10.1029/2003WR002068.

Blondeaux, P., and G. Seminara (1985), A unified bar bend theory of river meanders, *J. Fluid Mech.*, *157*, 449–470, doi:10.1017/S0022112085002440.

California Department of Water Resources (CDWR) (2001), Merced River Salmon Habitat Enhancement Project Phase III—Robinson Reach, engineering report, Sacramento.

California Department of Water Resources (CDWR) (2006), The Merced River Salmon Habitat Enhancement Project Robinson Reach (Phase III) 2004 geomorphic monitoring report, Sacramento.

Camporeale, C., P. Perona, A. Porporato, and L. Ridolfi (2007), Hierarchy of models for meandering rivers and related morphodynamic processes, *Rev. Geophys.*, *45*, RG1001, doi:10.1029/2005RG000185.

Constantine, C. R., T. Dunne, and G. J. Hanson (2009), Examining the physical meaning of the bank erosion coefficient used in meander migration modeling, *Geomorphology*, *106*(3–4), 242–252, doi:10.1016/j.geomorph.2008.11.002.

Crosato, A. (2009), Physical explanations of variations in river meander migration rates from model comparison, *Earth Surf. Processes Landforms*, *34*(15), 2078–2086, doi:10.1002/esp.1898.

Darby, S. E., A. M. Alabyan, and M. J. Van de Wiel (2002), Numerical simulation of bank erosion and channel migration in meandering rivers, *Water Resour. Res.*, *38*(9), 1163, doi:10.1029/2001WR000602.

de Moor, J. J. W., R. T. van Balen, and C. Kasse (2007), Simulating meander evolution of the Geul River (the Netherlands) using a topographic steering model, *Earth Surf. Processes Landforms*, *32*(7), 1077–1093, doi:10.1002/esp.1466.

Dietrich, W. E. (1987), Mechanics of flow and sediment transport in river bends, in *River Channels: Environment and Process*, edited by K. S. Richards, pp. 179–227, Blackwell, New York.

Dietrich, W. E., and D. J. Smith (1983), Influence of the point bar on flow through curved channels, *Water Resour. Res.*, *19*(5), 1173–1192, doi:10.1029/WR019i005p01173.

Dietrich, W. E., and P. J. Whiting (1989), Boundary shear stress and sediment transport in river meanders of sand and gravel, in *River Meandering*, *Water Resourc. Monogr.*, vol. 12, edited by S. Ikeda and G. Parker, pp. 1–50, AGU, Washington, DC.

Dietrich, W. E., J. D. Smith, and T. Dunne (1979), Flow and sediment transport in a sand bedded meander, *J. Geol.*, *87*(3), 305–315, doi:10.1086/628419.

Duan, J. G., and P. Y. Julien (2005), Numerical simulation of the inception of channel meandering, *Earth Surf. Processes Landforms*, *30*(9), 1093–1110, doi:10.1002/esp.1264.

Engelund, F. (1974), Flow and bed topography in channel bends, *J. Hydraul. Div., Am. Soc. Civ. Eng.*, *100*(NHY11), 1631–1648.

Ergenzinger, P. (1992), Discussion of "Boundary shear stress and roughness over mobile alluvial beds" by Peter J. Whiting and William E. Dietrich (December, 1990, vol. 116, no. 12), *J. Hydraul. Eng.*, *118* (5), 818–821, doi:10.1061/(ASCE)0733-9429(1992)118:5(818.2).

Ferguson, R. I., D. R. Parsons, S. N. Lane, and R. J. Hardy (2003), Flow in meander bends with recirculation at the inner bank, *Water Resour. Res.*, *39*(11), 1322, doi:10.1029/2003WR001965.

Fischer-Antze, T., N. R. B. Olsen, and D. Gutknecht (2008), Three-dimensional CFD modeling of morphological bed changes in the Danube River, *Water Resour. Res.*, *44*, W09422, doi:10.1029/2007WR006402.

Hardy, R. J., S. N. Lane, R. I. Ferguson, and D. R. Parsons (2003), Assessing the credibility of a series of computational fluid dynamic simulations of open channel flow, *Hydrol. Processes*, *17*(8), 1539–1560, doi:10.1002/hyp.1198.

Howard, A. D., and T. R. Knutson (1984), Sufficient conditions for river meandering: A simulation approach, *Water Resour. Res.*, *20*(11), 1659–1667, doi:10.1029/WR020i011p01659.

Ikeda, S. (1989), Sediment transport and sorting at bends, in *River Meandering*, *Water Resourc. Monogr.*, vol. 12, edited by S. Ikeda and G. Parker, pp. 103–126, AGU, Washington, D.C.

Ikeda, S., G. Parker, and K. Sawai (1981), Bend theory of river meanders. 1. Linear development, *J. Fluid Mech.*, *112*, 363–377, doi:10.1017/S0022112081000451.

Johannesson, H., and G. Parker (1989), Linear theory of river meandering, in *River Meandering*, *Water Resour. Monogr.*, vol. 12, edited by S. Ikeda and G. Parker, pp. 181–214, AGU, Washington, D. C.

Lancaster, S. T., and R. L. Bras (2002), A simple model of river meandering and its comparison to natural channels, *Hydrol. Processes*, *16*(1), 1–26, doi:10.1002/hyp.273.

Lanzoni, S., and G. Seminara (2006), On the nature of meander instability, *J. Geophys. Res.*, *111*, F04006, doi:10.1029/2005JF000416.

Legleiter, C., and P. Kyriakidis (2006), Forward and inverse transformations between Cartesian and channel-fitted coordinate systems for meandering rivers, *Math. Geol.*, *38*(8), 927–958, doi:10.1007/s11004-006-9056-6.

Legleiter, C. J., and P. C. Kyriakidis (2008), Spatial prediction of river channel topography by kriging, *Earth Surf. Processes Landforms*, *33*(6), 841–867, doi:10.1002/esp.1579.

Legleiter, C. J., P. C. Kyriakidis, R. R. McDonald, and J. M. Nelson (2011), Effects of uncertain topographic input data on two-dimensional flow modeling in a gravel bed river, *Water Resour. Res.*, doi:10.1029/2010WR009618, in press.

Lewin, J. (1976), Initiation of bed forms and meanders in coarse-grained sediment, *Geol. Soc. Am. Bull.*, *87*(2), 281–285, doi:10.1130/0016-7606(1976)87<281:IOBFAM>2.0.CO;2.

Li, S., R. Millar, and S. Islam (2008), Modelling gravel transport and morphology for the Fraser River gravel reach, British Columbia, *Geomorphology*, *95*(3–4), 206–222, doi:10.1016/j.geomorph.2007.06.010.

Lisle, T. E., H. Ikeda, and F. Iseya (1991), Formation of stationary alternate bars in a steep channel with mixed-size sediment—A flume experiment, *Earth Surf. Processes Landforms*, *16*(5), 463–469, doi:10.1002/esp.3290160507.

Lisle, T. E., J. M. Nelson, J. Pitlick, M. A. Madej, and B. L. Barkett (2000), Variability of bed mobility in natural, gravel-bed channels and adjustments to sediment load at local and reach scales, *Water Resour. Res.*, *36*(12), 3743–3755, doi:10.1029/2000WR900238

Madej, M. A. (1999), Temporal and spatial variability in thalweg profiles of a gravel-bed river, *Earth Surf. Processes Landforms*, *24*(12), 1153–1169, doi:10.1002/(SICI)1096-9837(199911)24:12<1153::AID-ESP41>3.0.CO;2-8.

Madej, M. A. (2001), Development of channel organization and roughness following sediment pulses in single-thread, gravel bed rivers, *Water Resour. Res.*, *37*(8), 2259–2272, doi:10.1029/2001WR000229.

Madej, M. A., D. G. Sutherland, T. E. Lisle, and B. Pryor (2009), Channel responses to varying sediment input: A flume experiment modeled after Redwood Creek, California, *Geomorphology*, *103*(4), 507–519, doi:10.1016/j.geomorph.2008.07.017.

May, C. L., B. Pryor, T. E. Lisle, and M. Lang (2009), Coupling hydrodynamic modeling and empirical measures of bed mobility to predict the risk of scour and fill of salmon redds in a large regulated river, *Water Resour. Res.*, *45*, W05402, doi:10.1029/2007WR006498.

Meyer, G. A. (2001), Recent large-magnitude floods and their impact on valley-floor environments of northeastern Yellowstone, *Geomorphology*, *40*, 271–290, doi:10.1016/S0169-555X(01)00055-1.

Mosselman, E. (1998), Morphological modelling of rivers with erodible banks, *Hydrol. Processes*, *12*(8), 1357–1370, doi:10.1002/(SICI)1099-1085(19980630)12:8<1357::AID-HYP619>3.0.CO;2-7.

Nelson, J. M., and R. R. McDonald (1996), Mechanics and modeling of flow and bed evolution in lateral separation eddies, technical report, U.S. Geol. Surv. Grand Canyon Monit. and Res. Cent., Flagstaff, Ariz.

Nelson, J. M., and J. D. Smith (1989a), Evolution and stability of erodible channel beds, in *River Meandering*, *Water Resourc. Monogr.*, vol. 12, edited by S. Ikeda and G. Parker, pp. 321–378, AGU, Washington, D. C.

Nelson, J. M., and J. D. Smith (1989b), Flow in meandering channels with natural topography, in *River Meandering*, *Water Resourc. Monogr.*, vol. 12, edited by S. Ikeda and G. Parker, pp. 69–102, AGU, Washington, D. C.

Nelson, J. M., S. J. Bennett, and S. M. Wiele (2003), Flow and sediment transport modeling, in *Tools in Fluvial Geomorphology*, edited by G. M. Kondolf and H. Piegay, pp. 539–576, John Wiley, New York.

Pitlick, J. (1993), Response and recovery of a sub-alpine stream following a catastrophic flood, *Geol. Soc. Am. Bull.*, *105*(5), 657–670, doi:10.1130/0016-7606(1993)105<0657:RAROAS>2.3.CO;2.

Rattray, J. M., and E. Mitsuda (1974), Theoretical analysis of conditions in a salt wedge, *Estuarine Coastal Mar. Sci.*, *2*, 375–394, doi:10.1016/0302-3524(74)90006-1.

Rinaldi, M., B. Mengoni, L. Luppi, S. E. Darby, and E. Mosselman (2008), Numerical simulation of hydrodynamics and bank erosion in a river bend, *Water Resour. Res.*, *44*, W09428, doi:10.1029/2008WR007008.

Ruther, N., and N. Olsen (2007), Modelling free-forming meander evolution in a laboratory channel using three-dimensional computational fluid dynamics, *Geomorphology*, *89*(3–4), 308–319, doi:10.1016/j.geomorph.2006.12.009.

Seminara, G. (2006), Meanders, *J. Fluid Mech.*, *554*, 271–297, doi:10.1017/S0022112006008925.

Seminara, G. (2010), Fluvial sedimentary patterns, *Annu. Rev. Fluid Mech.*, *42*(1), 43–66, doi:10.1146/annurev-fluid-121108-145612.

Shimizu, Y., H. Yamaguchi, and T. Itakura (1990), Three-dimensional computation of flow and bed deformation, *J. Hydraul. Eng.*, *116*(9), 1090–1108, doi:10.1061/(ASCE)0733-9429(1990)116:9(1090).

Shiono, K., T. L. Chan, J. Spooner, P. Rameshwaran, and J. H. Chandler (2009a), The effect of floodplain roughness on flow structures, bedforms and sediment transport rates in meandering channels with overbank flows: Part I, *J. Hydraul. Res.*, *47*(1), 5–19, doi:10.3826/jhr.2009.2944-I.

Shiono, K., T. L. Chan, J. Spooner, P. Rameshwaran, and J. H. Chandler (2009b), The effect of floodplain roughness on flow structures, bedforms and sediment transport rates in meandering channels with overbank flows: Part II, *J. Hydraul. Res.*, *47*(1), 20–28, doi:10.3826/jhr.2009.2944-II.

Smith, J. D., and S. R. McLean (1984), A model for flow in meandering streams, *Water Resour. Res.*, *20*(9), 1301–1315, doi:10.1029/WR020i009p01301.

Struiksma, N., K. W. Olesen, C. Flokstra, and H. J. DeVriend (1985), Bed deformation in curved alluvial channels, *J. Hydraul. Res.*, *23*(1), 57–79, doi:10.1080/00221688509499377.

Vasquez, J. A., P. M. Steffler, and R. G. Millar (2008), Modeling bed changes in meandering rivers using triangular finite elements, *J. Hydraul. Eng.*, *134*(9), 1348–1352, doi:10.1061/(ASCE)0733-9429(2008)134:9(1348).

Whiting, P. J. (1997), The effect of stage on flow and components of the local force balance, *Earth Surf. Processes Landforms*, *22*(6), 517–530, doi:10.1002/(SICI)1096-9837(199706)22:6<517::AID-ESP707>3.0.CO;2-M.

Whiting, P. J., and W. E. Dietrich (1990), Boundary shear stress and roughness over mobile alluvial beds, *J. Hydraul. Eng.*, *116*(12), 1495–1511, doi:10.1061/(ASCE)0733-9429(1990)116:12(1495).

Whiting, P. J., and W. E. Dietrich (1991), Convective accelerations and boundary shear-stress over a channel bar, *Water Resour. Res.*, *27*(5), 783–796, doi:10.1029/91WR00083.

Wormleaton, P. R., R. D. Hey, R. H. J. Sellin, T. Bryant, J. Loveless, and S. E. Catmur (2005), Behavior of meandering overbank channels with graded sand beds, *J. Hydraul. Eng.*, *131*(8), 665–681, doi:10.1061/(ASCE)0733-9429(2005)131:8(665).

Yen, C., and B. Yen (1971), Water surface configuration in channel bends, *J. Hydraul. Div. Am. Soc. Civ. Eng.*, *97*(HY2), 303–321.

T. Dunne, Bren School of Environmental Science and Management, University of California, 3510 Bren Hall, Santa Barbara, CA 93106-5131, USA.

L. R. Harrison, Institute for Computational Earth System Science, University of California, 1324 Bren Hall, Santa Barbara, CA 93106-3060, USA.

C. J. Legleiter, Department of Geography, University of Wyoming, 1000 E. University Ave., Department 3371, Laramie, WY 82071, USA. (Carl.Legleiter@uwyo.edu)